Photocatalytic degradation of methylene blue using sunlight-powered coordination polymers constructed from a tetracarboxylate linker

Adetola C. Oladipo[a,b], Abiodun D. Aderibigbe[c], Victoria T. Olayemi[b,d], Peter A. Ajibade[e], Hadley S. Clayton[f], Pavel N. Zolotarev[g], Guy J. Clarkson[h], Richard I. Walton[h] and Adedibu C. Tella[b,f]

[a]Department of Physical Sciences, Landmark University, P. M. B 1001, Omu-Aran, Kwara State, Nigeria

[b]Department of Chemistry, P.M.B.1515, University of Ilorin, Ilorin, Kwara State, Nigeria

[c]Department of Chemistry, Federal University of Technology, P.M.B. 704, Akure, Ondo state, Nigeria

[d]Department of Chemistry, College of Pure and Applied Sciences, Kwara State University, P.M. B 1530, Malete, Nigeria.

[e]School of Chemistry and Physics, University of Kwazulu-Natal, Scottsville, Pietermaritzburg, 3209, South Africa.

[f] Department of Chemistry, University of South Africa, South Africa

[g]Università degli studi di Milano, Dipartimento di Chimica, Via Golgi 19, 20133 Milano, Italy

[h]Department of Chemistry, University of Warwick, Coventry, CV4 7AL, UK

Abstract

Here, we report the preparation of three coordination polymers - $[Mn_2(btec)]_n$, **1**; $[Ce_2(H_2btec)(btec)(H_2O)_2]_n$, **2**; and $[Fe(Hbtec)(H_2O)_2]_n$ **3** from 1,2,4,5-benzenetetracarboxylic acid (H_4btec). Physicochemical characterization of the coordination polymers was undertaken using microanalysis, X-ray crystallography, FTIR, PXRD, TGA/DSC, and UV/visible spectrophotometry to confirm the identities of the compounds. The Mn(II) centres in **1** exhibit octahedral geometry coordinated by six oxygen atoms and crystallizes in the monoclinic space group *I*2/*m*. In **2**, Ce(III) centres adopt tricapped trigonal prism geometry, coordinated by three $btec^{4-}$, three from H_2btec^{2-} and the oxygen from one coordinated water molecule. It crystallizes in the triclinic space group $P\bar{1}$. **3** is composed of an Hbtec ion and two water molecules coordinated to the Fe (III) ion. The band gaps of **1**, **2**, and **3** are 2.87, 3.10, and 3.61 eV, respectively, while their hydrogen peroxide-assisted efficiencies for the photodegradation of methylene blue are 91,

94, and 100% respectively. An active species trapping experiment showed that an increase in hydroxy radicals (•OH) explains the enhanced efficiencies and provide an insight into the mechanism of the photodegradation of methylene blue by the photocatalysts. Efficiencies of mixtures of **2**/H_2O_2 and **3**/H_2O_2 reduced only slightly over five cycles of use and PXRD data revealed that **2** and **3** were chemically stable over the three cycles. Overall, the coordination polymers could serve as potential candidates for industrial-scale methylene blue degradation in the aqueous phase.

Keywords: Photocatalysis, coordination polymers, methylene blue, Fenton process, band gap, 1,2,4,5-benzenetetracarboxylic acid.

1.0 Introduction

Dyes are important raw materials in the textile and paper industries, but also constitute a major group of contaminants in wastewater from these industries [1]. Dyes in waterbodies reduce solar light penetration efficiency which results in a reduction in photosynthesis, an increase in biological oxygen demand, and absence of dissolved oxygen for aquatic life [2]. Synthetic dyes, particularly derivatives bearing aromatic rings, like methylene blue, are relatively inert to heat, oxidizing agents, and light, making removal from wastewater rather challenging [3]. Therefore, the need to protect aquatic flora and fauna, and ultimately human and environmental health and to operate a circular production process necessitate efficient, cheap, and easy-to-operate industrial wastewater decontamination technologies. Contemporary wastewater decontamination technologies like chemical oxidation [4], flocculation [5], bio-filtration [6], phytoremediation [7], sedimentation [8], precipitation [9], adsorption [10–12], and photocatalysis [13] have been widely adopted both on small and large scales with varying successes. Amongst these technologies, photocatalysis is unique because of its attractive features of being ‘green’, relatively easy to operate, and requirement for mild operational conditions [14].

Photocatalysis is the light energy-powered acceleration of a chemical reaction in the presence of a catalyst. In a typical photocatalytic process, light energy causes the promotion of an electron from the valence band (VB) of the photocatalyst into the conduction band (CB) leaving behind a corresponding hole in the VB [15]. The electrons in the CB and holes in the VB either migrate to the photocatalyst surface or recombine to achieve oxidation and reduction reactions respectively [16]. Titanium dioxide (TiO_2) is the most utilized photocatalyst for dye photodegradation. While

TiO_2 is reactive, chemically stable, and available at a relatively low cost, it is responsive mainly to ultraviolet (UV) light due to its wide band gap [17]. To undertake photocatalytic degradation of dyes using natural sunlight, it is imperative to develop new photocatalysts with excellent efficiencies under visible light irradiation, which is the largest region of the solar spectrum. Consequently, a variety of materials has been investigated such as metal oxides [18], metal sulfides [19], metal nanoparticles [20], and coordination polymers (CPs) [21].

CPs which are supramolecular structures of metals linked by organic ligands through coordinate bonds, stand out due to important properties like the possibility of huge internal surface area and tunable pore size [22]. Metal-organic frameworks (MOFs) are a sub-class of CPs that have the potential for such porosity. CPs are suitable for use as photocatalysts for degrading organic pollutants due to their suitable HOMO-LUMO band gap leading to desirable band gaps. The ligands increase the light absorption ability and transfer energy to metal via ligand to metal charge transfer (LMCT). They are superior to traditional inorganic photocatalysts as they absorb in the visible region and show active response upon visible light excitation [23]. Another remarkable property of CPs is the possibility of tuning their light absorption properties, invariable their band gap, to suit the intended use by careful selection of the precursors and modification of the organic linker [24]. The band gap is related to ligand-to-metal charge transfer (LMCT), which occurs at specific wavelengths under light irradiation, depending on the nature of organic linkers and metals in the CP. CPs have been employed for photocatalytic degradation of dyes with some interesting results [25,26]. For instance, a 3D Zr-MOF prepared using carboxylic acid functionalized porphyrin linkers in a dimethylformamide-acetic acid-water media showed a band gap of 2.77 eV and a dye degradation of nearly 100% over a five-hour cycle [27]. Semerci's group described the synthesis of a Cd-based CP with a band gap of 3.99 eV, where the CP functioned under UV/visible light irradiation for methylene blue degradation, with an efficiency of 60% [21]. Zhang and coworkers reported the preparation and application of a copper-based 2D MOF photocatalyst for methylene blue degradation. This photocatalyst was constructed using 1-(tetrazo-5-yl)-4-(triazo-1-yl) benzene organic linker, had a band gap of 2.21 eV, and photodegraded methylene blue with an efficiency of 91% under UV light irradiation [28].

It is widely reported that the photocatalytic efficiency can be enhanced by the addition of H_2O_2 which serves as both an electron acceptor to suppress the electron-hole recombination; and also a source of highly reactive hydroxyl radical to degrade organic pollutants into less toxic products

[29]. The use of H_2O_2 as the terminal oxidant in oxidation processes is favoured due to its environmentally benign nature with water as its by-product.

In recent times, photocatalysts are increasingly required to demonstrate excellent efficiency under a broad spectrum of light energy like that from natural sunlight. Although the intensity of natural sunlight varies with implications for experimental reproducibility on a laboratory scale, this light source is potentially cheap and easy to employ on an industrial scale. Additionally, natural sunlight is a renewable resource, and its use could add to the green credentials of photocatalysis. The development of highly efficient solar-driven photocatalysts is still one of the most important goals pursued by scientists [30,31]. Interestingly, studies reporting on photocatalytic degradation of dyes under natural sunlight are emerging. As an illustration, Luo's group showed that under natural sunlight irradiation with an average intensity of 760 – 840 Wm^{-2}, iron(III)-based 3D CP/graphene oxide composite, neat iron(III)-based 3D CP, and graphene oxide photocatalysts photodegraded methylene blue with efficiencies of 100% in 20, 40, and 50 min, respectively [32]. Under natural sunlight irradiation, Etaiw and coinvestigators reported that a mixture of Pb(II) CP, with a band gap of 3.49 eV, as a photocatalyst, and hydrogen peroxide, as oxidant, was observed to photodegrade methylene blue with an efficiency of 91.1% [33]. In a different study, Etaiw's team communicated that a combination of a Mn-based CP, with a band gap of 2.06 eV, and hydrogen peroxide degraded 72.6% of the initial eosin-Y dye concentration under natural sunlight illumination in 180 min [34]. It is encouraging to find that there are CP photocatalysts with demonstrated efficiencies for dye degradation under natural sunlight and it is natural to expect that these could be considered for scaling up for industrial application. For all the rapid and excellent photodegradation observed, we noted that some of the synthesis protocols of some of the photocatalysts in the studies discussed above were elaborate. Therefore, we considered if other CPs with facile synthesis, in commonly available and green solvents like water, could show similar or better degradation efficiencies. Also, we considered how the band gap relates to efficiency under natural sunlight irradiation. Finally, we sought to understand the mechanism of the photodegradation process.

Herein, we describe the syntheses of three new CPs – $[Mn_2(btec)]_n$, **1**; $[Ce_2(H_2btec)(btec)(H_2O)_2]_n$, **2**; and $[Fe(Hbtec)(H_2O)_2]_n$ **3**, using the ligand 1,2,4,5-benzenetetracarboxylic acid (H_4btec) (Figure 1). The choice of Mn, Ce, and Fe as metal centres stems from studies revealing that metals with

multiple oxidation states often form supramolecular structures with semiconductor properties and function as photocatalysts with high chemical stability [35,36]. Additionally, Mn, Ce, and Fe salts have relative low toxicity and cost [37,38]. H_4btec was selected as the organic ligand for several important considerations. First, the highly delocalized π electrons promote the LMCT transitions and reduce the electronic band gap of the CPs **1** – **3** which is important for access to visible-light powered CP-based photocatalysts [14]. Secondly, it has a strong coordination ability which could provide high thermal and chemical stabilities to the resulting CPs. Finally, it is water soluble, and bears numerous binding modes to metal ions arising from fully or partially deprotonation, affording a wide variety of CP structures [39]. CPs **1**, **2**, and **3** were prepared in water in one step. Following extensive characterizations, the CPs were applied as heterogeneous photocatalysts for the degradation of methylene blue under natural sunlight. The addition of hydrogen peroxide as an oxidant to the Fe-based photocatalyst was required to achieve complete degradation of the dye. Put together, the facile synthesis and relative thermal and chemical stabilities, present the Fe-based photocatalyst for potential application in industrial photodegradation of methylene blue in the aqueous phase.

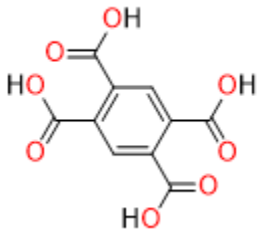

Figure 1. Structure of 1,2,4,5-benzenetetracarboxylic acid (H_4btec)

2.0 Experimental Details

2.1 Materials

$Mn(NO_3)_2{\cdot}4H_2O$, $Ce(CH_3COO)_3{\cdot}H_2O$, $FeCl_3{\cdot}9H_2O$, 1,2,4,5-benzenetetracarboxylic acid (H_4btec), methanol, TiO_2 (PC 50), methylene blue (MB) dye, HCl (37%), NaOH pellets (97%), EDTA, NaOH, isopropanol and H_2O_2 were purchased from commercial sources and used without further purification.

2.2 Syntheses

$[Mn_2(btec)]_n$, 1. A mixture of $Mn(NO_3)_2{\cdot}4H_2O$ (251 mg, 1 mmol) and H_4btec (254 mg, 1 mmol) in distilled H_2O (10 mL) was placed in a 20 mL Teflon-lined autoclave and heated at 120 ºC for 4

days (Figure S1). After the mixture was slowly cooled to room temperature, pale yellow crystals were obtained. Yield: 72%. Molecular weight: 360 g/mol. Melting point: 402 ºC. Anal. Calc. for $C_{10}H_2O_8Mn_2$ (%): C, 33.33; H, 0.06; Found: C, 32.34. IR, (KBr, cm^{-1}): 2234, 1650, 1502, 1434,1311, 558, 466. UV-Vis. (diffuse-reflectance) ($\lambda_{intraligand}$, nm): 270, 304;(λ_{LMCT}, nm): 407; ($\lambda_{d\text{-}d}$, nm): 520.

$[Ce_2(H_2btec)(btec)(H_2O)_2]_n$, 2. The synthesis was similar to that described in **1** except that $Ce(CH_3COO)_3 \cdot H_2O$ (317 mg, 1 mmol) was used for **2** instead of $Mn(NO_3)_2 \cdot 4H_2O$. Also, the reaction time was 2 days for **2** instead of 4 days for **1**. Yellow crystals were obtained, separated, washed with methanol, and dried in air for 20 minutes. Yield: 78 %. Molecular weight 818 g/mol. Melting point: 510 ºC. Anal. Calc. for $C_{20}H_{10}O_{18}Ce_2$ (%): C, 28.91; H, 1.35; Found: C, 29.34; H, 1.22. IR, (KBr, cm^{-1}): 3512, 2922, 1669, 1579, 1460,1348, 818 669, 445. UV-Vis. (diffuse-reflectance) ($\lambda_{intraligand}$, nm): 256, 315; (λ_{LMCT}, nm): 396.

$[Fe(Hbtec)(H_2O)_2]_n$, 3. The synthesis was similar to that described for **1** except that $FeCl_3 \cdot 9H_2O$ (90 mg, 0.33 mmol) was used for **3** instead of $Mn(NO_3)_2 \cdot 4H_2O$, and the reaction time was 2 days. The yellow powder obtained was filtered, washed with methanol, and dried in the oven at 80 ºC for 30 minutes (Scheme 3.5). Yield: 89 %, Molecular weight 342 g/mol; Melting point: 316 ºC; Anal. Calc. for $C_{10}H_6O_{10}Fe$ (%): C, 34.93; H, 2.02; Found: C, 35.02; H, 2.06; IR, (KBr, cm^{-1}): 3405, 1683, 1496, 1395, 1142 659, 455. UV-Vis. (diffuse-reflectance) ($\lambda_{intraligand}$, nm): 254, 310; (λ_{LMCT}, nm): 368.

2.3 Instrumentation

C, H, and N microanalyses were carried out with a PerkinElmer 2400 element analyzer. Scanning electron microscopy images were recorded on a Philips (FEI) XL30 microscope. Transmission electron micrographs were recorded on JOEL JEM 1400 microscope. IR spectra were recorded in KBr discs on a Bruker Vertex 70 V IR Spectrometer in the 4000- 450 cm^{-1} region. The solid-state diffuse-reflectance UV/vis spectra for powder samples were recorded with a Cary UV/vis spectrophotometer equipped with an integrating sphere by using $BaSO_4$ as a white standard, whereas the UV/Vis spectra for solution samples were acquired using Beckman U730 spectrophotometer. The powder XRD data were obtained on a Siemens D5000 diffractometer operating with Cu Kα1/2 radiation over the 2θ range of 5–35º in flat-plate geometry. TGA/DSC was carried out on a Mettler Toledo 1-600 thermal analyzer under flowing N_2 with a heating rate

of 10 °C/min between ambient temperature and 800 °C. For the X-ray crystallographic analysis, a single crystal was chosen and mounted in Fomblin oil onto thin glass fibre after which X-ray intensity data were measured at 150(2) K on an Xcalibur Gemini diffractometer with Cu-Kα radiation (λ = 1.54184 Å) and a Ruby CCD area detector. Using Olex2 [40], structures were solved with the ShelXT [41] structure solution program using Intrinsic Phasing and refined with the ShelXL [42] refinement package using Least Squares Minimisation. Photoluminescence spectroscopy was done with Renishaw 1000 InVia Raman Microscope using 325 nm excitation laser beams within the wavelength range of 200-800 nm.

2.4 Photocatalytic Degradation Procedure

A suspension of powdered catalysts (50 mg of **1**, **2**, **3**, or TiO_2) in a fresh aqueous solution of MB dye (10 mg/L, 100 mL) at varying pH was continuously stirred, first in the dark for 30 min (to establish an adsorption-desorption equilibrium of dye on the catalyst surface) and later under solar irradiation with an average illuminance of 13.5 LUX. At the start of the experiment and given intervals during the experiment, 5 mL suspensions were withdrawn, centrifuged (to remove suspended catalyst particles) and the filtrate was analyzed using a UV/Vis spectrophotometer. The concentration of the dye was measured by taking the absorbance at 665 nm, which is the wavelength of maximum absorption (λ_{max}) of the MB dye chromophore. The efficiency of the catalysts for the dye degradation was evaluated as C/C_0 at different time intervals and the percentage degradation was calculated by using the equation:

$$Degradation\ (\%) = \frac{C_0 - C}{C_0}\ x\ 100$$

where C_0 is the initial concentration of dye and C is the final concentration of dye at a given time. Active species trapping experiments (ASTE) were carried out using the photocatalytic degradation procedure as described above, but in addition, EDTA, silver nitrate, and isopropanol were added in separate reaction set-ups, as scavengers for holes, electrons, and hydroxyl radicals respectively. The concentrations of the EDTA and $AgNO_3$ were 1 mmol/L and the volume of isopropanol used was 0.1 mL. For the reusability measurement, after each degradation cycle, the photocatalyst was filtered off the suspension and washed with 1 mol/L HNO_3 aqueous solution and deionized water to remove the adsorbed dye molecules from the photocatalyst surface, followed by centrifuging and drying at 105 ^oC for 24 hours.

3.0 Results and discussion

3.1 Description of the crystal structures

Crystal data and structure refinement parameters of $[Mn_2(btec)]_n$ **1** and $[Ce_2(H_2btec)(btec)(H_2O)]_n$ **2** are given in Table S1. Selected bond distances and angles are presented in Table S2. $[Mn_2(btec)]_n$ crystallizes in the monoclinic space group *I*2/*m*. The ORTEP diagram of **1** is given in Figure 2a. It shows that **1** is made up of chains of $[Mn_2(btec)]_n$ with benzenetetracarboxylate (btec) acting as a bridging ligand. The asymmetric unit contains half an Mn and a quarter of a 1,2,4,5-tetracarboxylate (Figure 2b). Within the carboxylate groups, one oxygen (O1) coordinates to Mn1 monodentately while the other (O2) serves as a bridge between Mn1 atoms. Bond distances of C2-O1 (1.250 Å) are shorter than that of C2-O2 (1.283 Å) due to the different coordination modes of the oxygen atoms. The Mn1 atom has an octahedral environment (MnO_6) with two O1 atoms and four O2 atoms. Oxygen atoms O1, O1, O2, and O2 reside at the corners of the basal plane and O2 atoms are located at the apical positions.

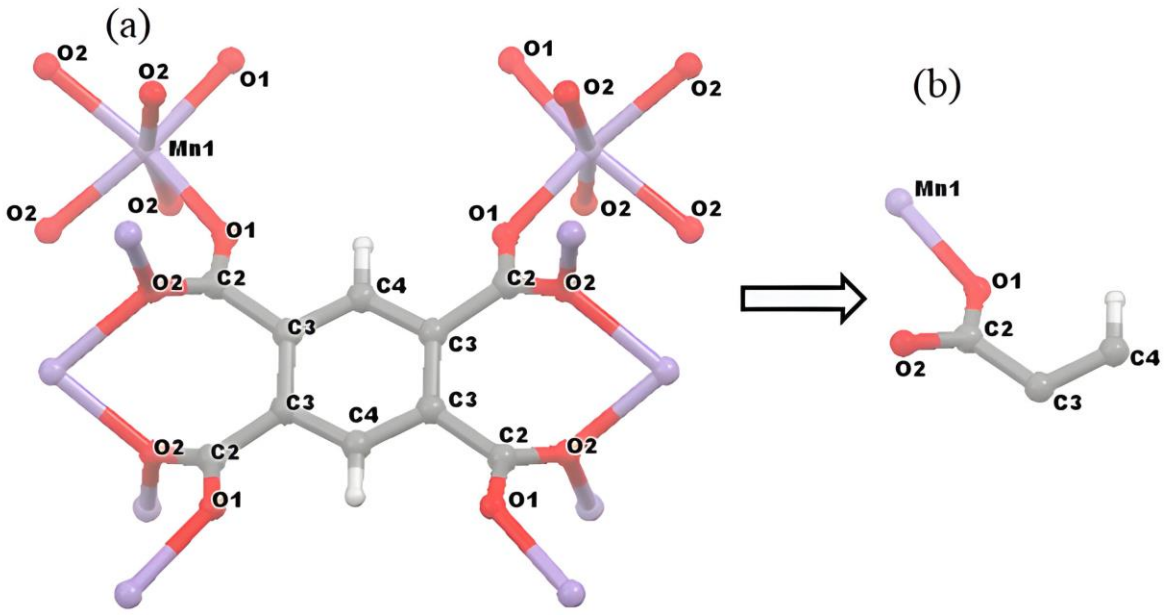

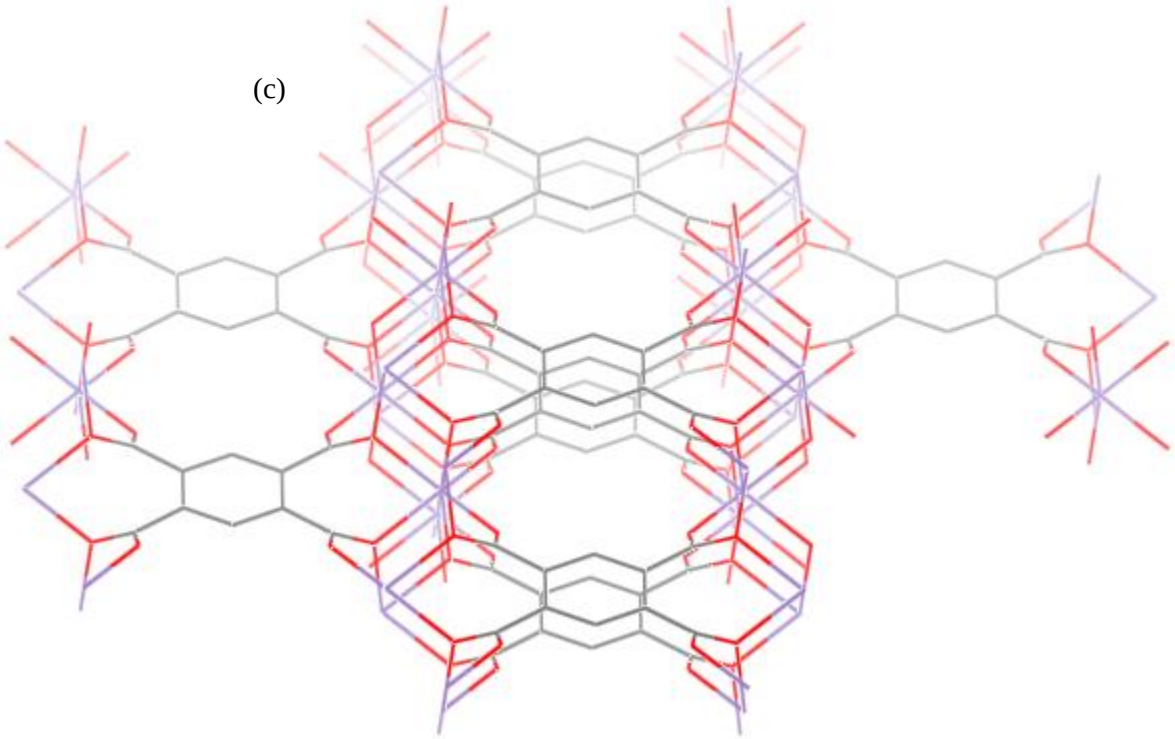

Figure 2. $[Mn_2(btec)]_n$ (**1**) (a) ORTEP diagram (b) Asymmetric unit with thermal ellipsoids drawn at 50 % probability level (c) 3D polymeric structure of **1**

The Mn-O (carboxylate) bond lengths in the range 2.1144(9) - 2.2369(9) Å and bond angles between 76.16(4) - 167.66(5)^o are in the range reported for some previous manganese (II)-carboxylate complexes [43,44]. The Mn1-O2 distance of one of the bridged Mn atoms is slightly longer than that of the other bridged Mn atom (2.2370 Å vs 2.1670 Å). The Mn1-O1 bond length is 2.114 Å. The Mn···Mn separation is 3.467 Å. The six oxygen around each Mn(II) ions are from carboxylate groups and each ligand binds to ten metal centres. Within the carboxylate groups, one oxygen (O1) coordinates to Mn1 monodentately while the other (O2) serves as a bridge between two Mn1 atoms. The Mn-O bonding arrangement leads to a 3-dimensional polymeric assembly (Figure 2c), showing polygonal pores of 5.958 Å (C4···C4 distance) and 7.441 Å (Mn1···Mn1 distance). Each chain connects to the next through a – O–Mn–O – net-type association and each Mn(II) cation is bridged by neighbouring ligands through the carboxylates.

A better understanding of the network structure was achieved using the ToposPro software [45] along with the TopCryst service [46], we get the standard representation [47] of **1** as 5,10-**fit**

underlying net with the Mn connecting to five different ligands (one chelate and four terminal) acting as 5-coordinated (Figure S7) and with the tetracaboxylate ligand linking to ten different Mn atoms as shown in Figure 2. There are 29 isoreticular coordination networks reported in TopCryst database and among them we found the isomorphous iron derivative (refcode MUBJUO, MUBJUO01) [48,49]

Single crystal analysis of **2** reveals a chemical formula $[Ce_2(H_2btec)(btec)(H_2O)]_n$ and a structure in which each cerium is coordinated by nine oxygen atoms (Figure 3a). Five of the oxygen atoms are from three $btec^{4-}$ ligands, three are from H_2btec^{2-} ligands and the last is from the oxygen of a coordinated water molecule to form a tricapped trigonal prism coordination environment. $[Ce_2(H_2btec)(btec)(H_2O)]_n$ crystallizes in the triclinic space group $P\bar{1}$. The asymmetric unit of **2** contains two half molecules of the ligand and water bound to a Ce ion (Figure 3b). There are two coordination modes of the ligands to the Ce ions (Supporting Information Figure S3). First, C102-C106 (H_2btec^{2-}) has the two para-deprotonated carboxylates using both oxygens of the carboxylate (O101 and O102) and the other two paraprotonated carboxylate groups ligate via the carbonyl oxygen (O106) and the other carboxylate oxygen O107, which is protonated. Secondly, tetracarboxylate C202-C206 ($btec^{4-}$) has two paradeprotonated carboxylates chelating Ce ions and one of the oxygen atoms of the other two paradeprotonated carboxylate (O201) bridges two Ce ions thereby exhibiting a chelating-bridging mode of coordination.

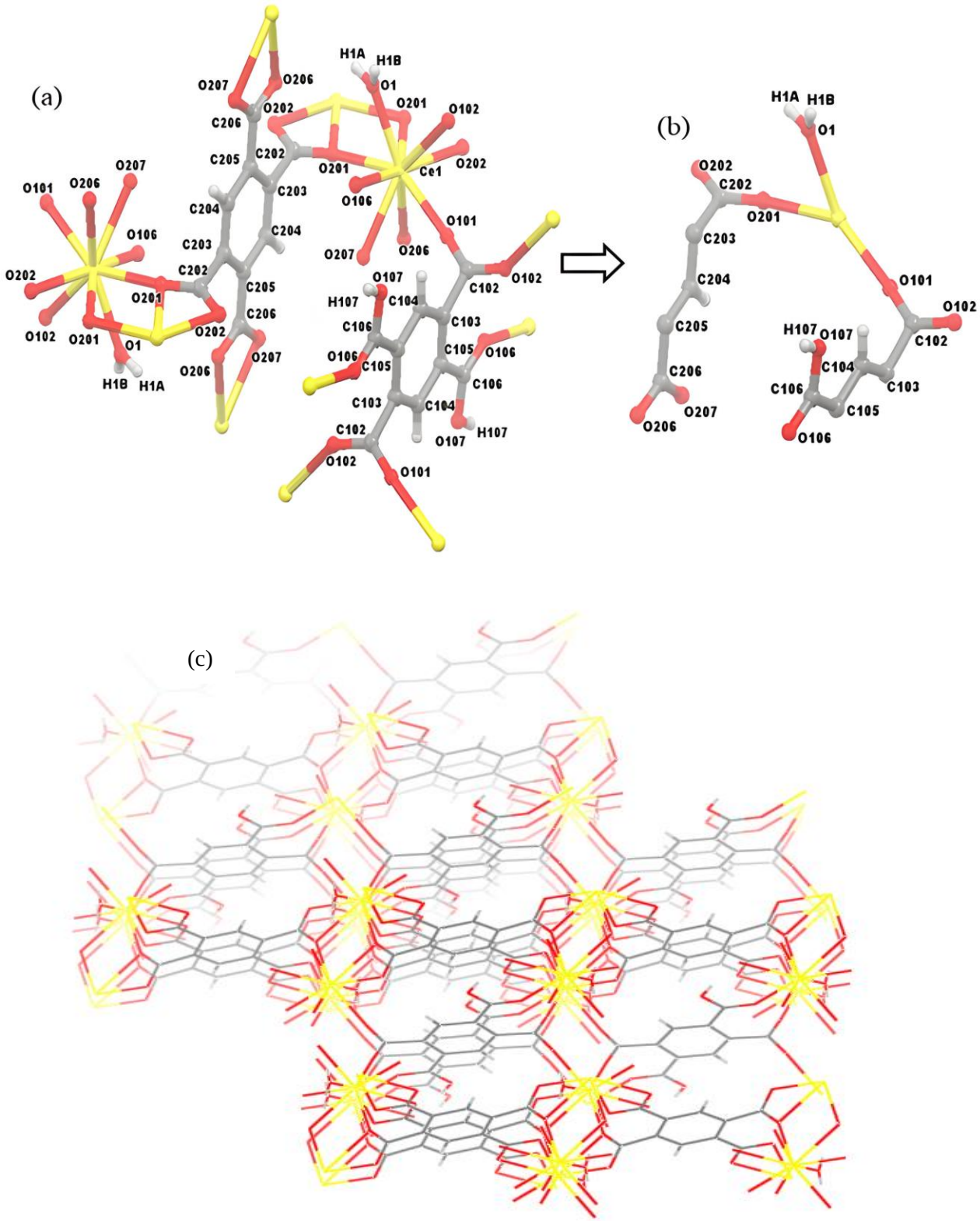
(a)
(b)
(c)
H1A
H1B
O1
O207
O206
O202
C206
C205
C202
O201
Ce1
O102
O101
O106
C203
C204
O107
H107
C104
C103
C105
C102

Figure 3 $[Ce_2(H_2btec)(btec)(H_2O)]_n$ (**2**) (a) ORTEP diagram (b) Asymmetric unit with thermal ellipsoids drawn at the 50 % probability level (c) Wireframe representation of the 3D structure of **2**

The Ce-O distances range from 2.4075(11) to 2.9453(3) Å and O-Ce-O angles between 50.53(3) - 145.54(4)^o and are comparable to reported Ce (III) compounds [50,51]. This structure is extended to a 3D framework (Figure 3c) because of the multicarboxylate ligand, which is already known to be capable of forming coordination compounds of high dimensionality [52,53]. The space within the framework is occupied by coordinated water molecules.

The high dimensionality of the framework is also aided by hydrogen bonds. Table S3 shows the hydrogen bond parameters, while Supporting Information Figure S4, shows how intermolecular hydrogen bonds are formed between the oxygen of the water molecule (O1) and the carboxylate oxygens (O202 and O206). The other hydrogen bonding interaction is between the protonated oxygen atom (O107) and the carboxylate oxygen atom (O207). These are likely to stabilize the framework rather than any strong pi-pi interactions, as the centroid-centroid distances, shown in Figure S5 are high and cannot support homo-interactions between the benzene rings.

For the topological analysis, **2** is the well known 6,6-**nia** (Nickel Arsenide) underlying net with the Ce connecting to six different ligands (Figure S6) and with the ligands linking to six different Ce atoms as shown in figure S2. There are 263 isoreticular coordination networks reported in TopCryst database and among them we found the Ce compound (refcode PIQSOX) [54].

Apart from **1** and **2** that were obtained in crystal forms and had their structures analysed by single crystal X-ray diffraction studies, powder form of **3** was obtained, all attempts to obtain single crystals were futile and so the structure was proposed after it was analysed using other characterization techniques namely CHN, XRD, TGA, FTIR and UV-Visible spectroscopic analyses.

3.2 FTIR

FTIR spectra were recorded to characterize bulk samples of the CPs and to identify the binding mode of H_4btec in the CPs (Figure 4a). Notable vibrational frequencies in the spectra of H_4btec are 3045 cm^{-1} (carboxylic O-H stretch) and a peak at 1690 cm^{-1} (asymmetric carboxylic C=O stretch for a dimer) [55]. The spectrum of **1** contains notable peaks at 1565 cm^{-1} and 1484 cm^{-1} representative of the asymmetric carboxylate (COO^-) and symmetric carboxylate (COO^-)

stretches respectively [55]. Compared to the spectrum of H_4btec, the absence of the carboxylic O-H stretching vibration in **1** and the shift of the asymmetric carboxylic C=O stretching vibrations to 1565 cm^{-1} is apparently due to complexation with Mn and verifies the binding mode of the ligands in **1** [56]. Furthermore, the absence of the carboxylic O-H peak in **1** show that all the carboxylate oxygens bound with Mn and this is consistent with the observed crystal structure of **1**. The spectra of **2** and **3** bear strong peaks at 3102 and 3137 cm^{-1} (carboxylic O-H stretch), 1711 and 1726 cm^{-1} (carboxylic C=O stretch of a free carboxylic group), 1594 and 1540 cm^{-1} (asymmetric carboxylate COO^{-} stretch) and 1484 and 1404 cm^{-1} (symmetric carboxylate COO^{-} stretch) respectively [55]. The presence of carboxylic C=O stretching vibrations at 1711 and 1726 cm^{-1} in **2** and **3** respectively reveals that not all the carboxylate oxygens are bound with metals [55]. The shift in the asymmetric carboxylic C=O stretching vibrations to 1594 and 1540 cm^{-1} in the spectra of **2** and **3**, compared to 1690 cm^{-1} provides evidence of ligand coordination in **2** and **3**. Finally, the splitting in the energy of the asymmetric and symmetric carboxylate stretching vibrations (Δ) is indicative of the carboxylate coordination binding mode in the CPs (**1**, **2**, and **3**) [57]. The asymmetric carboxylate stretching vibrations of **1**, **2**, and **3** are located at 1565, 1594, and 1540 cm^{-1} respectively, and the corresponding symmetric stretching vibrations are situated at 1484, 1425, and 1404 cm^{-1}. Therefore for **1**, the splitting energy (Δ) of 81 cm^{-1} shows a chelating binding which means that both carboxylate oxygens form a covalent bond with one Mn [58]. This is consistent with some of the binding modes observed in the crystal structure of **1** in Figure 2a. The binding modes for **2** and **3** are bridging bidentate from the calculated Δs of 169 and 140 cm^{-1} respectively [58]. This means that each carboxylate oxygen covalently binds to a different metal ion, in this case, Ce. The crystal structure of **2** (Figure 2a) supports this.

3.3 Thermal properties (TGA and DSC)

The thermal properties were investigated using TGA and DSC to determine the thermal stability of the CPs. The TGA trace of CP **1** revealed one weight loss step of 57% (56.11 % calculated) between 400 – 500 ^{o}C indicating the combustion of the benzenetetracarboxylate (btec). This loss is represented in the corresponding DSC curve by an exothermic peak of high intensity (Figure 4b). The Mn (II) becomes oxidized to Mn (III), giving 43% of Mn_2O_3 (43.59 % calculated) as residue, stable till 800 ^{o}C . In contrast, the trace of CP **2** shows two different weight loss steps across the same temperature range. The first weight loss of 3.6% (4.4 % calculated), attributed to

loss of water molecules, was observed in the 250 – 330 ^{o}C range. The DSC curve bears a low-intensity exothermic peak. The second step loss of 54.35 % (55.5 % calculated), rationalized as the combustion of the ligands, was observed between 330 and 510 ^{o}C, and this loss is accompanied by a large exothermic peak. Ce_2O_3 residue was stable up to 800 ^{o}C and this accounts for the remaining 42% (40.1 % calculated) of the total weight. CP **3** shows two weight loss steps, with an initial loss of 6% between 180 and 320 ^{o}C, which can be assigned as due to the evaporation of coordinated water molecules. The later loss of 67% starting at 330 until 400 ^{o}C represents combustion of btec. Overall, **3** lost 73% of its original weight across the temperature range and the DSC curve bears two exothermic peaks. The traces show that **1** and **3** have the highest and lowest first onset decomposition temperatures respectively (**3**: 180 ^{o}C, **2**: 250 ^{o}C, **1**: 400 ^{o}C, Figure 4b).

3.4 PXRD

PXRD patterns were obtained to determine the purity of the CPs. Both simulated and experimental PXRD patterns of **1** and **2** (Figure 4c) are similar and confirm the purity of the bulk materials, with no evidence for any unreacted starting materials in either. The PXRD pattern of **3** which was obtained in powder form was observed to be different starting from that of the starting material H_4btec (Figure 4c), indicating the formation of a new material. The pattern also does not match any known Fe(III)-btec material earlier reported [59–61].

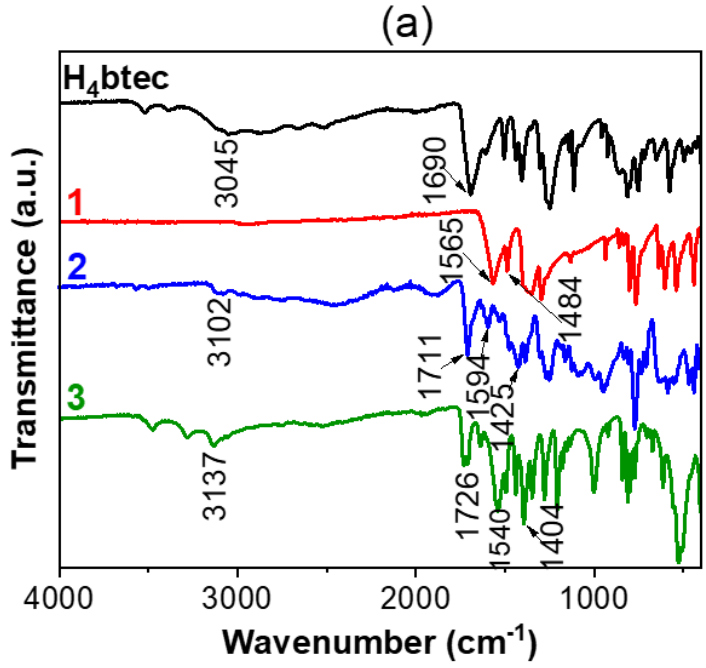

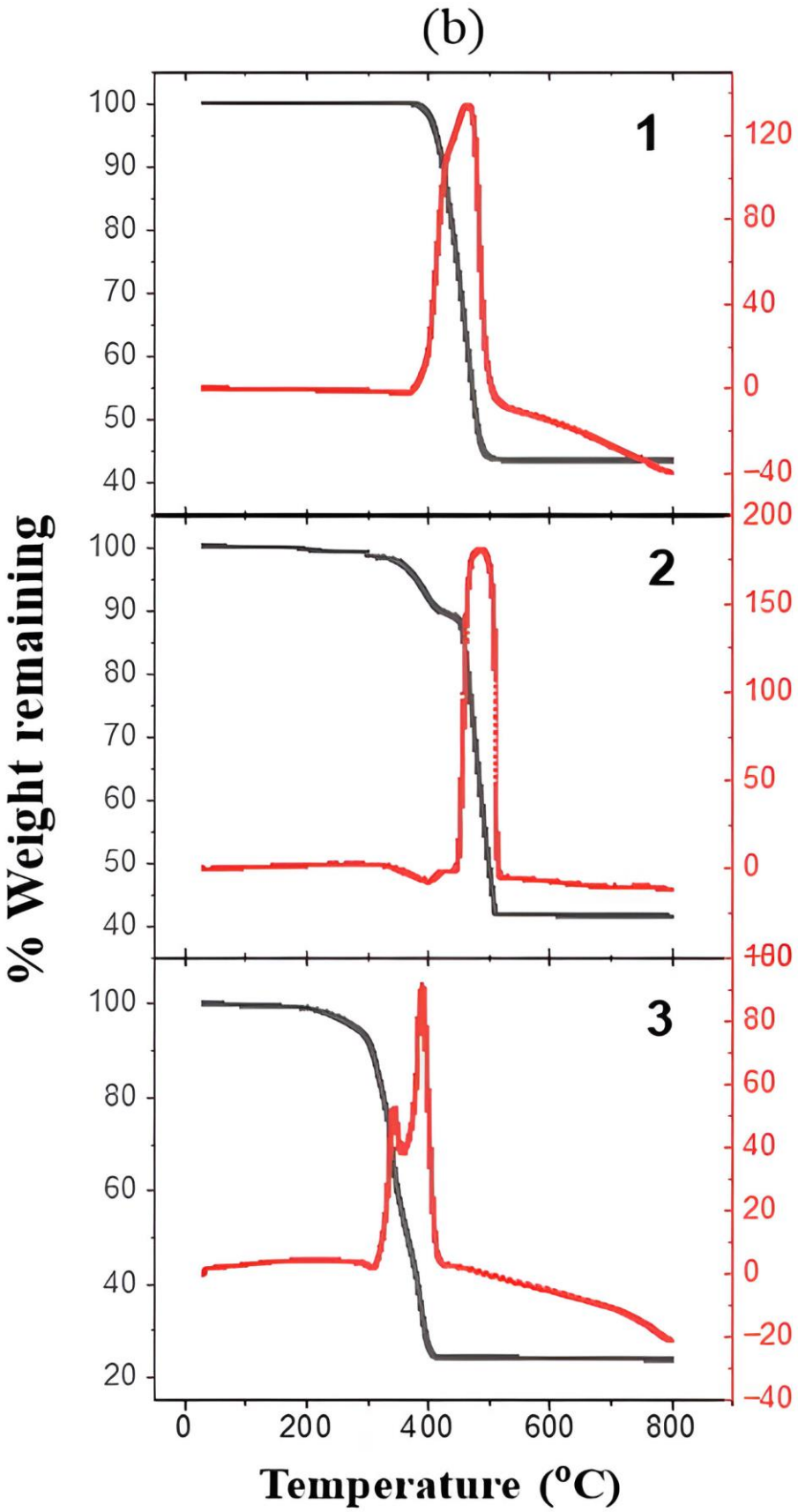
(b)
1
2
3
% Weight remaining
Temperature (°C)
100
90
80
70
60
50
40
120
80
40
0
−40
200
150
100
50
0
−100
80
60
40
20
0
−20
−40
20
0
200
400
600
800

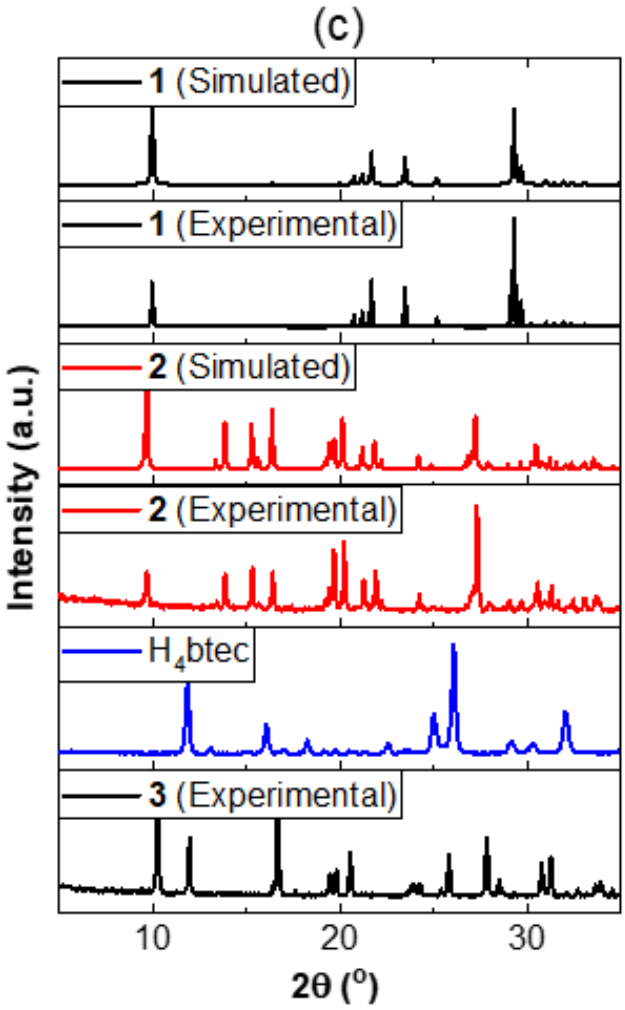

Figure 4. Physicochemical characterization of **1**, **2**, and **3**, (a) FTIR, (b) TGA/DSC, and (c) PXRD

3.5 TEM

The morphologies and diameters were determined using TEM micrographs. All CPs appear as chain-like aggregates of nearly spherical particles (Figures 5a – c). The average diameters were found to be (41.8±5.3), (40.0±3.8), and (46.7±3.2) nm for CP **1**, **2**, and **3** respectively.

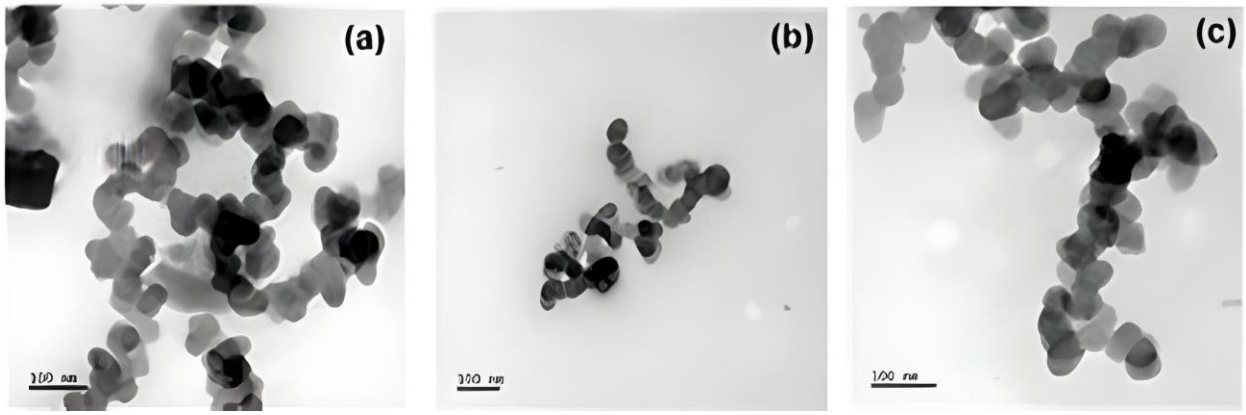

Figure 5. Transmission electron microscopy (TEM) micrographs of CP (a) **1**, (b) **2**, and (c) **3**

3.6 Photocatalytic Characteristics

The UV-Vis diffuse reflectance spectra show the light absorption properties of CPs **1**, **2**, and **3** (Figure 6a), and all spectra contain absorption components representative of π-π^* and n-π^* transitions. In addition, the absorption peaks at 419, 396, and 368 nm for **1**, **2**, and **3,** respectively, are characteristic of ligand-to-metal charge transfer (LCMT) from the p-orbitals of the carboxylate oxygen of the ligand to the valence orbitals of the corresponding metal ions. Other observed transitions are detailed in Supplementary Information Table S4. The semiconductor characteristics of the prepared compounds are a function of the band gaps (E_g) which were measured from the UV-Vis diffuse reflectance spectra and determined from Tauc plots, a plot of $(\alpha hv)^2$ and photon energy (hv) based on the energy dependency correlation equation, $\alpha hv = (hv - E_g)^{1/2}$, where α and E_g are absorption coefficient and band gap respectively. In a typical Tauc plot, the band gap is the intercept on the hv axis (where $\alpha = 0$) of a straight line extending from the linear portion of the plot [62]. From Figure 6b, the band gaps of **1**, **2**, and **3** are determined to be 2.87, 3.10, and 3.61 eV respectively whereas the band gap of PC50 has been documented to be 3.2 eV [63]. The fact that the measured E_g of the CPs is less than 4.00 eV, which is within the range for a semiconductor material, inspired us to investigate behaviors of **1**, **2**, and **3** in the heterogenous photocatalytic degradation of MB.

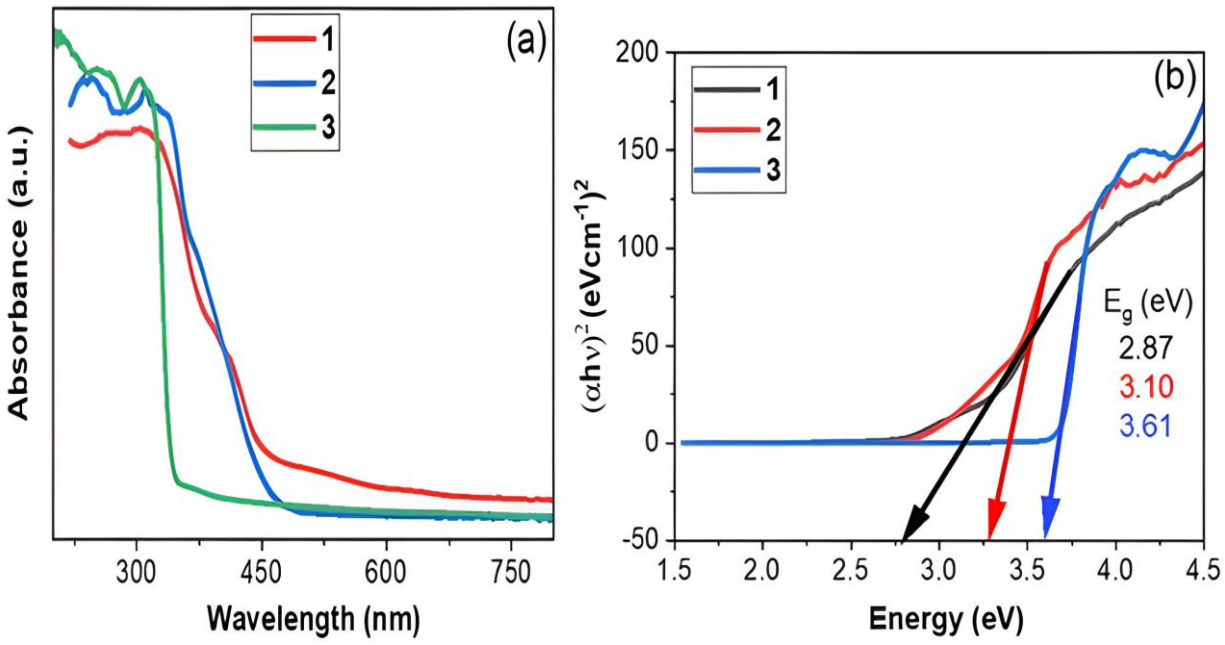

Figure 6. (a) UV/Vis diffuse reflectance spectra and (b) Tauc plots for **1**, **2**, and **3**.

Herein, we chose a thiazine organic dye – methylene blue (MB) (Figure 7), as a target pollutant for degradation experiments to assess the photocatalytic performance of CPs **1**, **2**, and **3**, noting that MB is a water-soluble dye bearing aromatic rings which are quite stable to natural degradation process.

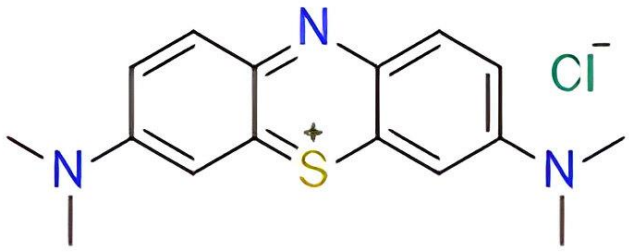

Figure 7. Molecular structure of methylene blue

The photodegradation experiment under visible light was undertaken following the achievement of the dark adsorption-desorption equilibrium. Control experiments to establish the importance of light irradiation and the use of the CP to facilitate the photodegradation of MB were carried out. The control experiment using the CPs in the dark and without H_2O_2 is shown on Figure 8. This

gives an insight into the adsorption of the dye on the CPs, and hence their porosity. There was an insignificant reduction in the concentration of the residual dye concentration in the dark (about 8%, 2% and 3% for CPs **1, 2** and **3** respectively) all through the duration of 150 minutes, indicating that the adsorptive removal of the dye on the CPs is negligible. Also, as expected, no observable degradation of MB occurred when irradiated by natural sunlight in the absence of photocatalysts **1**, **2**, and **3** (Figure 8). These results show that the presence of both light irradiation and the CPs **1**, **2**, and **3** are necessary for the degradation of MB.

The comparison of the photocatalytic study of the CPs under visible light irradiation is presented in Figure 8. Clearly, **3** showed the best photocatalytic activity with a degradation efficiency of 55% within 150 min, albeit with a slow degradation at the beginning of irradiation. Though **2** exhibited a fast initial degradation, it demonstrated an efficiency of 31% after 150 min, which is the next best efficiency to **1**. CP **1** was observed to degrade MB with an efficiency of 28%, the least of the three CPs. Put together, the order of photocatalytic activity is in the order **1** < **2** < **3**.

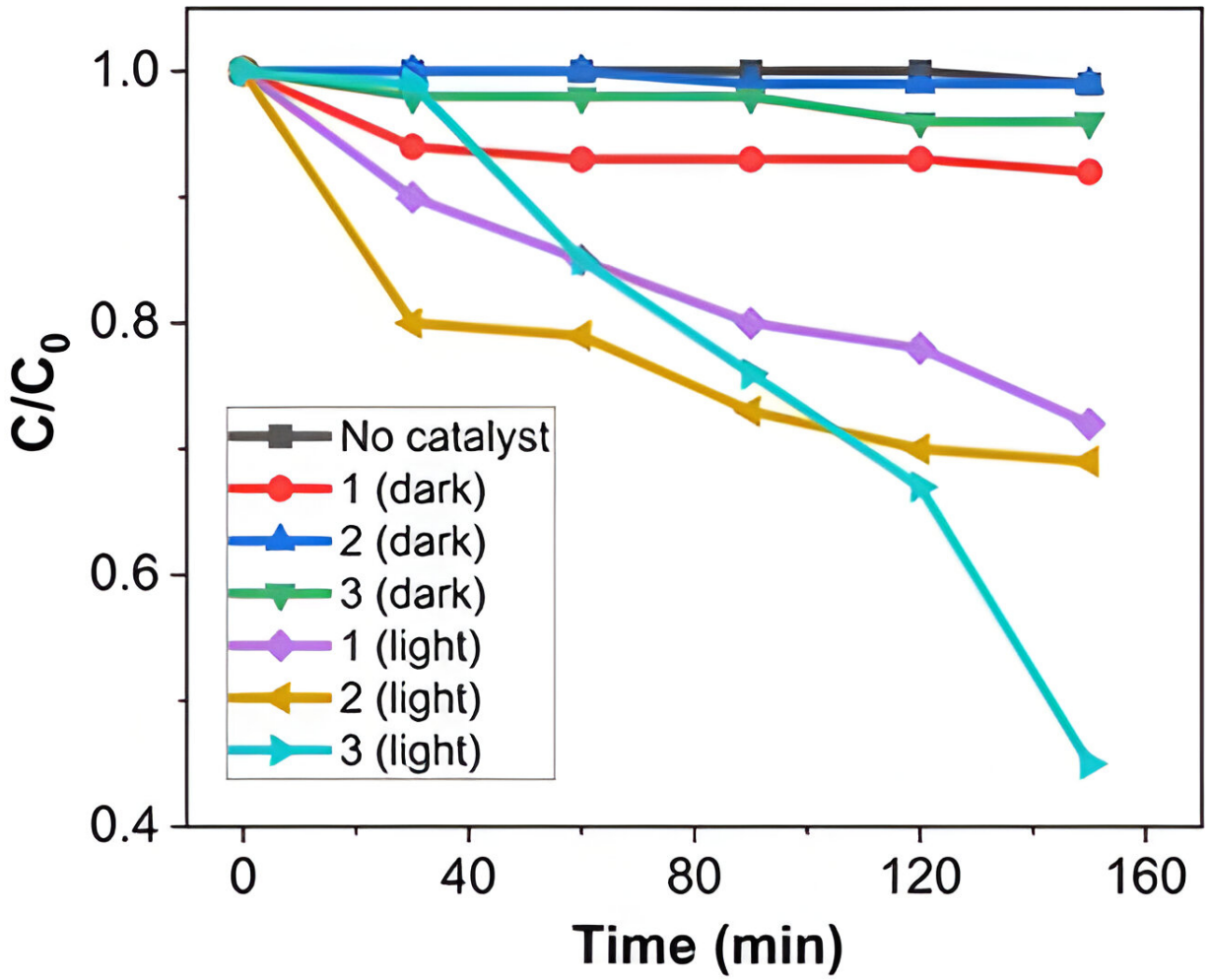

Figure 8. Degradation profiles of methylene blue with/without irradiation in the presence of CPs **1**, **2**, and **3**.

The generally low degradation efficiencies of the materials could be linked to the rapid recombination of the photogenerated electrons (e^-s) and the holes (h^+s) and this reduces the excitons available for oxidation of organic molecules [64]. To confirm this, photoluminescence (PL) analysis was undertaken, as PL signals are related to the recombination rate of the electron and hole and therefore, can be used to gain insight into the rate of recombination of the photo-induced species [65,66]. For the PL measurement of the three photocatalysts, the emission wavelength was 325 nm. Excitation wavelengths were 626, 525, and 719 nm for **1**, **2**, and **3**, respectively, with different intensities. As shown in Figure S7, the PL emission intensity is in the order: **1** > **2** > **3**. A low intensity of a PL signal indicates that the photogenerated species recombine slowly [67]. Consequently, the charge recombination rate follows the order **3** < **2** < **1**, which is

consistent with the MB degradation efficiency results observed. To slow down the charge recombination rate and enhance the photocatalytic activities of **1**, **2**, and **3**, H_2O_2 was employed as an inorganic oxidant. H_2O_2 limits charge recombination rate by accelerating the release of hydroxyl radicals (•OH) which scavenges photogenerated electrons. Preliminary experiments show that irradiation is important for the photocatalytic activity of the combination of any of **1**, **2**, and **3** (Figure 8), evidenced by the reduction in MB concentration over the entire duration of the experiment. A comparison of the MB degradation performances of the CPs with H_2O_2 revealed that H_2O_2 afforded better degradation efficiency (Figure 9) attributed to •OH generated according to Equations 1 – 3. The combination of each of **1**, **2**, and **3** separately with H_2O_2, symbolized as **1**/H_2O_2, **2**/H_2O_2, and **3**/H_2O_2 respectively, under irradiation showed improved degradation efficiency compared to neat **1**, **2**, and **3** (Figure 9). For example, the combination of **1** and H_2O_2 symbolized as '**1**/H_2O_2' degraded 91% of the initial MB compared to the 28% degraded by neat **1**. Also, **2**/H_2O_2 and **3**/H_2O_2 reduced the initial MB concentration by 94 and 100% respectively compared to the 31 and 55% observed for neat **2** and **3** respectively. The photocatalyst mixture of **3**/H_2O_2 demonstrated the best MB degradation efficiency just like **3** performed best amongst the CPs, highlighting the excellent photocatalytic ability of **3**.

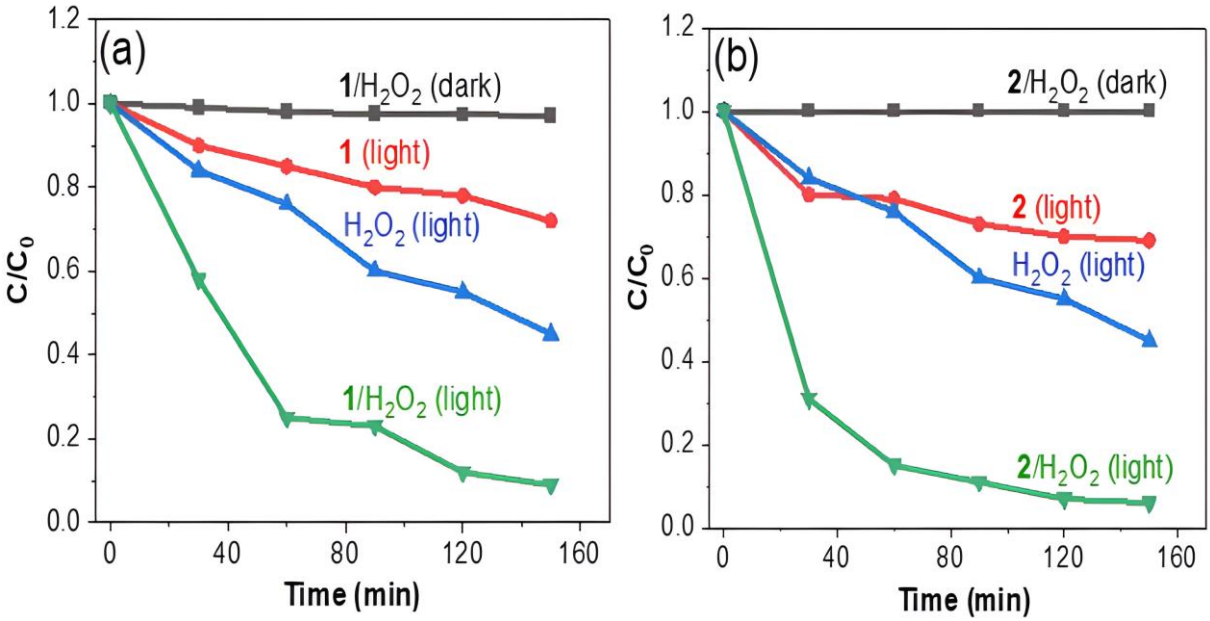

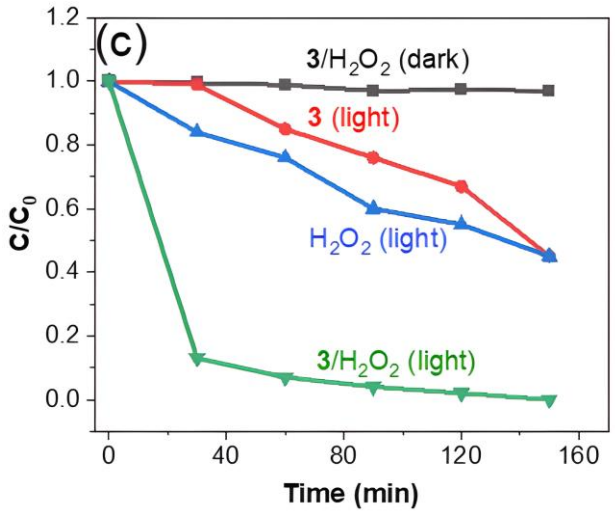

Figure 9. Enhancing effect of H_2O_2 on photocatalytic activity of (a) **1**, (b) **2**, and (c) **3** for methylene blue (MB) degradation as a function of irradiation time.

The kinetic data are well modeled by the apparent pseudo-first order rate equation, $-\ln(C/C_0) = kt$, where k is the rate constant, C and C_0 are the concentration of MB at irradiation time t and $t = 0$, respectively (Figure S8). The rate constants under visible light illumination are displayed in Table 1.

Table 1. Rate constants for the degradation of methylene blue using **1**, **2**, and **3** and the mixtures with H_2O_2.

Photocatalyst	**Rate constant, *k* (min^{-1}) x 10^{-2}**
H_2O_2 (only)	0.52
1	0.22
2	0.14
3	0.61
1/H_2O_2	1.61
2/H_2O_2	1.35
3/H_2O_2	2.06

The calculated rate constants reveal that: (a) H_2O_2 provided a better degradation rate than each of **1**, **2**, and **3**, (b) **1**/H_2O_2, **2**/H_2O_2, and **3**/H_2O_2 gave higher degradation rates than neat **1**, **2**, and **3** respectively, showing a synergistic enhancement for degradation by each of **1**, **2**, and **3** separately with H_2O_2. The synergistic index (SI), a measure of the synergistic effect was determined by

$$SI = \frac{k_{(photocatalyst/H_2O_2)}}{k_{(photocatalyst)}+k_{(H_2O_2)}},$$

where, $k_{(photocatalyst/H_2O_2)}$, $k_{(photocatalyst)}$, and $k_{(H_2O_2)}$ are rate constants for (**1**/H_2O_2, **2**/H_2O_2, or **3**/H_2O_2), neat CP (**1**, **2**, or **3**) and H_2O_2 respectively. A synergistic effect is in operation when the calculated SI value is greater than 1 [68]. The calculated SI values for the **1**/H_2O_2, **2**/H_2O_2 and **3**/H_2O_2 systems are 2.18, 2.04 and 1.82, showing the synergistic effect of each of **2** and **3** with H_2O_2 for the degradation of MB.

Table 2 displays the efficiencies of some CP-based photocatalysts (with/without H_2O_2) for the degradation of MB under UV, visible or natural sunlight. An holistic consideration of the light source, initial concentration and volume of the MB solution, degradation percentage and the irradiation time of various reported CP-based photocatalysts and the reported CPs in this work shows that CPs **2** and **3** have comparable, and in some cases, higher efficiencies compared to previously reported materials. Noteworthy is the large volume of MB dye degraded using CPs **2** and **3**, compared to reported works shown on the table. More desirably, the relatively cheap precursors, low toxicity of the metals and the green route synthesis are other advantages of CPs **2** and **3** over the reported materials.

Table 2: Performance evaluation of **2** and **3** in MB photodegradation compared to other literature materials.

CP-based photocatalyst	Light source	Initial concentration (ppm)/Volume of MB solution	Degradation efficiency (%)	Irradiation time (min)	Reference
$Cu(4,4'\text{-bipy})Cl]_n$ (H_2O_2 - assisted)	Visible	10 (40mL)	93.93	150	[62]
$[Co(4,4'\text{-bipy})\cdot(HCOO)_2]_n$ (H_2O_2 - assisted)	Visible	10 (40mL)	54.70	150	[62]
Mn-MOF of 1,5–naphthalene disulphonic acid and 4,4′ -bipyridine	Visible	10 (50mL)	63	60	[69]
Mn-MOF of 1,5–naphthalene disulphonic acid and 4,4′ -bipyridine (H_2O_2 - assisted)	Visible	10 (50mL)	90	25	[69]
Zn-MOF of 2,6-naphthalene disulphonic acid and 4,4'-bipyridine	Visible	10 (50mL)	63	50	[29]
Zn-MOF of 2,6-naphthalene disulphonic acid and 4,4'-bipyridine (H_2O_2 - assisted)	Visible	10 (50mL)	98	25	[29]
Nitrogen-doped quantum-ZIF-8-dot	Sunlight	14 (100mL)	93	180	[70]
$\{[Cu_2(TTB)(SO_4)(OH)]\cdot H_2O\cdot MeCN\}n$	UV	10 (50mL)	80.1	60	[71]
$[Na_2Zn_3(btc)_2(\mu\text{-}HCOO)_2(\mu\text{-}H2O)_8]_n$	Sunlight	15 (30mL)	93.69	80	[72]
$[Na_2Zn_3(btc)_2(\mu\text{-}HCOO)_2(\mu\text{-}H2O)_8]_n$ (composited with ZnO)	Sunlight	15 (30mL)	97.53	80	[72]
$[Ce_2(H_2btec)(btec)(H_2O)]_n$ (H_2O_2 - assisted)	Sunlight	10 (100mL)	94	150	This work
$[Fe(Hbtec)(H_2O)_2]_n$ (H_2O_2 - assisted)	Sunlight	10 (100mL)	100	150	This work

4,4′-bipy - 4,4′-bipyridine; HTTB - 1-(tetrazo-5-yl)-4-(triazo-1-yl) benzene; H_3btc = benzene tricarboxylic acid

3.7 Mechanism of MB Degradation

Mechanistically, photocatalytic activity is considered to proceed following the semiconductor concept which suggests that UV/vis illumination of photocatalysts having band gaps not up to 4.00 eV results in the generation of charge carriers, including h^+ and e^-, because of excitation of photocatalyst electrons from the valence to the conduction band [73]. The photocatalytic process also involves the creation of reactive oxygen species from the charge carriers, namely hydroxyl radical (•OH) from the capture of an electron from water by h^+, superoxide radical ($\bullet O_2^-$) following the reaction of e^- with oxygen [74]. However, when the photocatalytic activity involves the addition of H_2O_2, the creation of •OH from e^-, $\bullet O_2^-$, and homolytic cleavage of H_2O_2 (Equation 1 – 3) may be observed. To understand the mechanism of the photocatalytic process in this study,

active species trapping experiments (ASTE) for the two most efficient photocatalysts, **2** and **3** in combination with H_2O_2 was undertaken, to ascertain which reactive species accounts for the photodegradation process. We decided to study the mechanism using **2**/H_2O_2 and **3**/H_2O_2 and not neat **2** and **3** because the former gave the best degradation efficiencies. Consequently, $AgNO_3$, Ethylenediaminetetraacetic acid (EDTA), and isopropanol (*i*PrOH) were employed as e^-, h^+, and •OH scavengers respectively, to limit the availability of these species for reaction with the target pollutants [74]. Results from the ASTE are displayed in Figures 10 a & b. In comparison to the degradation rates of **2**/H_2O_2 and **3**/H_2O_2, the use of a photocatalyst mixture containing EDTA (**2**/H_2O_2/EDTA and **3**/H_2O_2/EDTA) led to a reduction in MB degradation rates (Figure 10a), which means h^+ is involved in the photodegradation process. Similarly, the degradation rates were reduced when **2**/H_2O_2/*i*PrOH and **3**/H_2O_2/*i*PrOH were used (Figure 10a), which suggests that •OH is involved in the photodegradation of MB. However, no noticeable change in degradation rates resulted from the use of $AgNO_3$ (Figure 10a) revealing either (a) H_2O_2 trapped the photogenerated e^-, leaving none to be trapped by $AgNO_3$ consistent with the improved degradation efficiencies recorded with the addition of H_2O_2 or (b) no e^- was generated in the photocatalytic process. Consequently, the $\bullet O_2^-$ may be uninvolved in the photodegradation process. Identical observations were observed for the ASTE of **3** (Figure 10b). The latter explanation (b) could not be true as band gap data show that **2** and **3** are true semiconductors. Therefore, the ASTE shows that •OH is involved in the MB degradation process consistent with the enhanced degradation efficiencies recorded when H_2O_2 was used.

With the understanding of the species responsible for the photocatalytic activity, it is deduced that H_2O_2 accelerates the hydroxyl radical creation rate by three means. First off, the self-breakdown of H_2O_2 by light irradiation results in hydroxyl radical creation (Equation 1). Next, H_2O_2 could function as a substitute electron acceptor to oxygen (Equation 2), which may limit the recombination of photogenerated holes and electrons. Finally, superoxide ($\bullet O_2^-$) could reduce H_2O_2 at the conductance band producing hydroxyl radical (Equation 3) [75].

$$H_2O_2 + h\nu \rightarrow 2 \bullet OH \qquad (1)$$

$$e_{CB}^- + H_2O_2 \rightarrow OH^- + \bullet OH \qquad (2)$$

$$\bullet O_2^- + H_2O_2 \rightarrow OH^- + \bullet OH + O_2 \qquad (3)$$

The highest degradation efficiency shown by **3**/H_2O_2 may be explained by the generation of additional hydroxyl radicals by H_2O_2 decomposition through the Fenton-like reaction, in other words, the Fe(III)-O clusters may have catalyzed the decomposition of H_2O_2 to give hydroxyl radicals (Equation 4 and 5) [76]. It is therefore noteworthy that the direct excitation of the Fe-O cluster could have contributed to the photocatalytic performance of **3**. A similar observation was reported by Laurier and coworkers [77]. CPs containing only Ce or Mn as metal centres have not been reported to demonstrate this behavior.

$$Fe^{3+} + H_2O_2 \rightarrow Fe^{2+} + \bullet O_2H + H^+ \quad (4)$$

$$Fe^{2+} + H_2O_2 \rightarrow Fe^{3+} + \bullet OH + OH^- \quad (5)$$

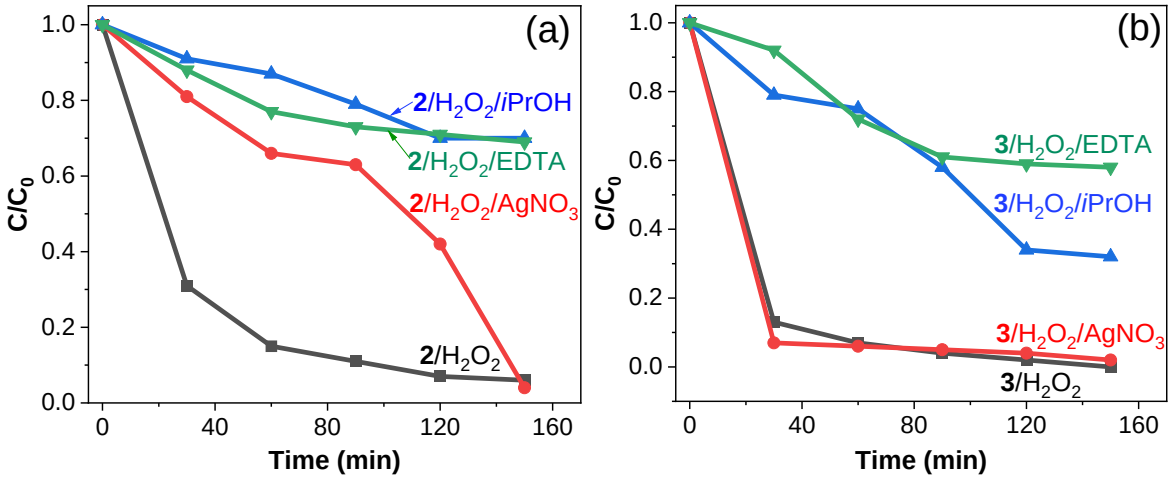

Figure 10. Effect of scavengers on the degradation of methylene blue using (a) **2** and (b) **3**.

3.8 Recyclability and chemical stability of the photocatalysts

To meet the demands of sustainability, functional materials like photocatalysts are required to have a prolonged life with constant efficiency and reusability properties linked to the chemical stability of the photocatalyst. However, CPs are generally unstable in the presence of water owing to the powerful interaction of the metal nodes with water molecules resulting in breakage of coordination bonds, the recyclability test of the CPs for MB degradation was undertaken. After five cycles, the degradation efficiencies using **2**/H_2O_2 and **3**/H_2O_2 were 86% and 90% respectively, indicating the

stability and reusability of the photocatalysts (Figure 11a). The amount of Fe (III) ion that leached into the solution after photocatalysis was quantified using the Atomic Absorption Spectrometer, to gain insight into the sample stability. 0.02 mg/L of Fe(III) was found in the test solution after the photocatalytic reaction, which shows that there was an insignificant metal-ion leaching from **3** into the solution. The stability of the photocatalysts was also monitored using X-ray powder diffraction. The powder XRD pattern of the **2** and **3** (Figure 11b) before and after the third photocatalysis reaction are identical. The FT-IR spectra of **2** and **3** (Figure S9) corroborates the stability of the photocatalysts as there are no changes in the spectra of the compounds after the experiment. These are indicators that the photocatalysts are stable, maintaining the structures under the experimental conditions.

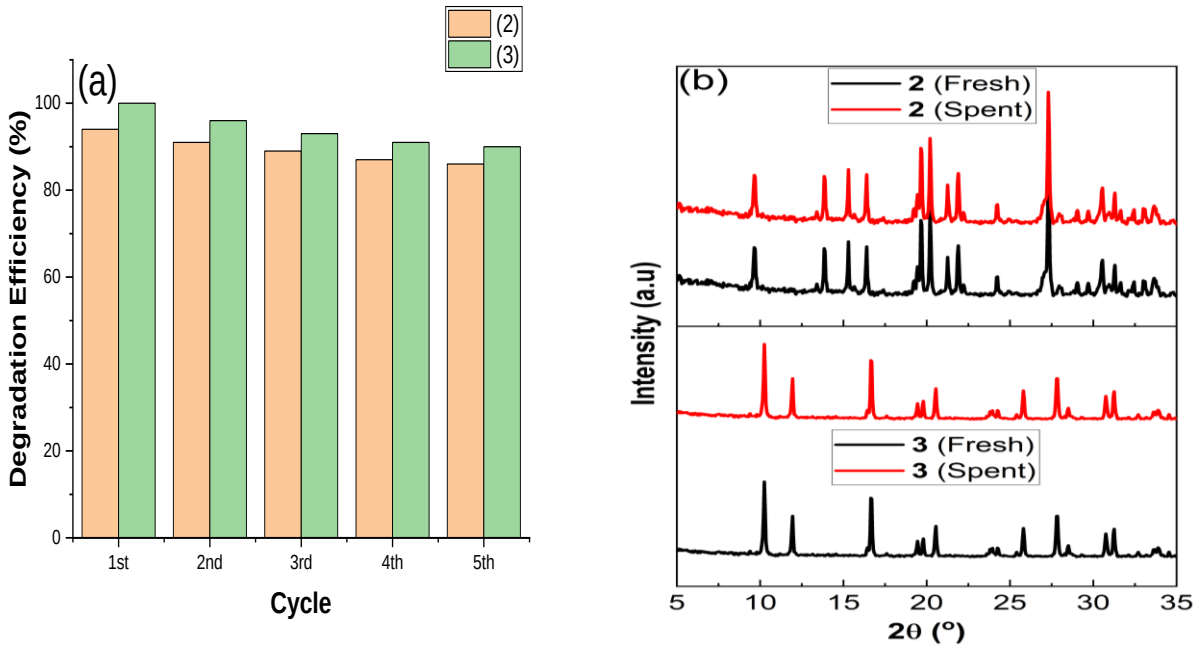

Figure 11. (a) Recyclability of CPs **1** and **2;** (b)XRD patterns of **2** and **3** before (fresh) and after the third cycle of methylene blue degradation (spent) to show the chemical stability of the photocatalysts.

4.0 Conclusion

Three new coordination polymers with the tetradentate 1,2,4,5-benzenetetrracarboxylic acid as organic linker precursor have been prepared in one simple step and observed to possess different structures and topologies, as expected for the different metal cations used. The band gaps are in the order **1** < **2** < **3**, with **3** showing the best, though moderate, efficiency for methylene blue degradation under natural sunlight irradiation. Photodegradation efficiencies of **2** and **3** were enhanced by the addition of hydrogen peroxide resulting in nearly complete and complete degradation of methylene blue respectively. The observed efficiencies of mixtures of **2** and **3** separately with hydrogen peroxide were also recorded following kinetic studies. Mechanistic studies undertaken by active specie trapping experiments revealed that •OH is involved in the photodegradation of methylene blue. Mixtures of **2** and **3** separately with hydrogen peroxide (**2**/H_2O_2 and **3**/H_2O_2) showed consistent efficiencies after five reuse cycles for methylene blue degradation and XRD results indicate that **2** and **3** are chemically stable after the fifth cycle of photodegradation. Overall, we have shown that coordination polymer type photocatalysts, prepared in a facile process can photodegrade methylene blue under natural sunlight irradiation. Results from this study have implications for the potential industrial application of photocatalysts for methylene blue-containing industrial wastewater.

Supplementary data

CCDC **1954759** and **2143127** contains the crystallographic data of $[Mn_2(btec)]_n$, **1** and $[Ce_2(H_2btec)(btec)(H_2O)_2]_n$, **2**, respectively. The data can be obtained free of charge from the Cambridge Crystallographic Data Centre via www.ccdc.cam.ac.uk/structures.

Conflict of Interest

The authors declare no conflict of interests.

CRediT authorship contribution statement

Adetola C. Oladipo: Conceptualization, Methodology, Data cu ration, Writing –original draft.

Abiodun D. Aderibigbe: Conceptualization, Methodology, Data curation, Writing –original draft.

Victoria T. Olayemi: Conceptualization, Methodology, Data curation, Writing –original draft.

Peter A. Ajibade: Formal analysis, Supervision, Funding acquisition, Writing –review & editing, Methodology, Supervision, Writing –review & editing.

Hadley S. Clayton: Formal analysis, Supervision, Funding acquisition, Writing –review & editing, Formal analysis, Investigation

Pavel N. Zolotarev: Topological analysis of the crystal structures

Guy J. Clarkson: Formal analysis, Investigation, X-ray crystallography analysis

Richard I. Walton: Formal analysis, Supervision, Funding acquisition, Writing –review & editing, Formal analysis, Investigation.

Adedibu C. Tella: Formal analysis, Supervision, Funding acquisition, Writing –review & editing, Methodology, Supervision, Writing –review & editing.

Acknowledgement

A.C. Oladipo is grateful to the Royal Society of Chemistry for the Researchers' Mobility Grant award, 2018, and we thank the University of Warwick's Research Technology Platforms for the provision of some of the facilities for the analysis of the compounds. P.N. Zolotarev thank the MUR for the grant PRIN2020 "Nature Inspired Crystal Engineering (NICE)".

References

[1] R. Al-Tohamy, S.S. Ali, F. Li, K.M. Okasha, Y.A.G. Mahmoud, T. Elsamahy, H. Jiao, Y. Fu, J. Sun, Ecotoxicol Env. Saf 231 (2022) 1–17.

[2] B. Lellis, C.Z. Fávaro-Polonio, J.A. Pamphile, J.C. Polonio, Biotechnol Res Innov 3 (2019) 275–290.

[3] C.X. Liu, W.H. Zhang, N. Wang, P. Guo, M. Muhler, Y. Wang, S. Lin, Z. Chen, G. Yang, Chem. - A Eur. J. 24 (2018) 16804–16813.

[4] A.C. Tella, A.C. Oladipo, V.O. Adimula, O.A. Ameen, S.A. Bourne, A.S. Ogunlaja, New J. Chem. 43 (2019) 14343–14354.

[5] E. Guibal, J. Roussy, React Funct Polym 67 (2007) 33–42.

[6] D.M. Jacklin, I.C. Brink, S.M. Jacobs, Water Sci Technol 84 (2021) 1715–1731.

[7] B. Bharathiraja, J. Jayamuthunagai, R. Praveenkumar, J. Iyyappan, Energy Environ. Sustain. Springer Nature, (2018) 243–252.

[8] A. Ouakouak, M. Abdelhamid, B. Thouraya, H.O. Chahinez, G. Hocine, N. Hamdi, A. Syafiuddin, R. Boopathy, Appl Sci 11 (2021) 1–18.

[9] Harish, P. Kumar, A. Soni, A.G. Chakinala, R. Singhal, R.P. Joshi, A.K. Mukhopadhyay, ChemistrySelect 7 (2022) 1–9.

[10] A.D. Aderibigbe, A.J. Clark, J Inorg Organomet Polym Mater 30 (2020) 4803–4808.

[11] A.C. Tella, A.C. Oladipo, V.O. Adimula, V.T. Olayemi, T.O. Dembaremba, A.S. Ogunlaja, G.J. Clarkson, R.I. Walton, Polyhedron 192 (2020) 114819.

[12] A.C. Oladipo, A.D. Aderibigbe, O.B. Akpor, T.O. Abodunrin, H.S. Clayton, A.C. Tella, J. Sulfur Chem. 44 (2023) 149–167.

[13] M. Rakibuddin, R. Ananthakrishnan, Sol Energy Mater Sol Cells 162 (201AD) 62–71.

[14] L. Wen, J. Zhao, K. Lv, Y. Wu, K. Deng, X. Leng, D. Li, Cryst Growth Des 12 (2022) 1603–1612.

[15] G. Boczkaj, A. Fernandes, Chem Eng J 320 (2017) 608–633.

[16] J. Harris, R. Silk, M. Smith, Y. Dong, W.T. Chen, G.I.N. Waterhouse, ACS Omega 5 (2020) 18919–18934.

[17] Y. Deng, C. Feng, L. Tang, G. Zeng, Z. Chen, M. Zhang, Nanohybrid Nanoporous Mater. Aquat. Pollut. Control. Elsevier (2018) 125–153.

[18] S. Kohtani, M. Koshiko, A. Kudo, K. Tokumura, Y. Ishigaki, A. Toriba, K. Hayakawa, R. Nakagaki, Appl Catal B 46 (2003) 573–586.

[19] F. Zhang, X. Wang, H. Liu, C. Liu, Y. Wan, Y. Long, Z. Cai, Appl Sci 9 (2019) 1–43.

[20] V.S.D. Devulapalli, R. Kushwaha, E. Ovalle, H.D. Singh, P. Shekhar, D. Chakraborty, C.P. Vinod, R. Vaidhyanathan, E. Borguet, ACS Appl Nano Mater 5 (2022) 4744–4753.

[21] A. Çiftlik, T.G. Semerci, O. Şahin, F. Semerci, Cryst Growth Des 21 (2021) 3364–3374.

[22] N.A. Khan, Z. Hasan, S.H. Jhung, J. Hazard. Mater. 244–245 (2013) 444–456.

[23] L. Wen, J. Zhao, K. Lv, Y. Wu, K. Deng, X. Leng, D. Li, Cryst. Growth Des. 12 (2012) 1603–1612.

[24] J. Gascon, M.D. Hernández-Alonso, A.R. Almeida, G.P.M. van Klink, F. Kapteijn, G. Mul, ChemSusChem 1 (2008) 981–983.

[25] J.-D. Xiao, H.-L. Jiang, Acc. Chem. Res. 52 (2019) 356–366.

[26] Q. Wang, Q. Gao, A.M. Al-Enizi, A. Nafady, S. Ma, Inorg. Chem. Front. 7 (2020) 300–339.

[27] K. Leus, T. Bogaerts, J. De Decker, H. Depauw, K. Hendrickx, H. Vrielinck, V. Van Speybroeck, P. Van Der Voort, Microporous Mesoporous Mater. 226 (2016) 110–116.

[28] F. Wang, F. Tian, Y. Deng, L. Yang, H. Zhang, D. Zhao, B. Li, X. Zhang, L. Fan, Cryst Growth Des 21 (2021) 4242–4248.

[29] T.K. Sindhu, R. Pavithran, A. Vidhya, J. Mol. Struct. 1245 (2021) 131039.

[30] D. Ye, L. Liu, Q. Peng, J. Qiu, H. Gong, A. Zhong, S. Liu, Molecules 28 (2023).

[31] X.-M. Huang, N. Chen, D.-N. Ye, A.-G. Zhong, H. Liu, Z. Li, S.-Y. Liu, Sol. RRL 7 (2023) 2300143.

[32] Y. Wu, H. Luo, H. Wang, RSC Adv. 4 (2014) 40435–40438.

[33] S.E. din H. Etaiw, D.M.A. El-Aziz, H. Marie, E. Ali, Solid State Sci. 79 (2018) 15–22.

[34] S.E. din H. Etaiw, H. Marie, Sens Actuators B Chem 290 (2019) 631–639.

[35] O. Fabelo, J. Pasán, L. Cañadillas-Delgado, F.S. Delgado, F. Lloret, M. Julve, C. Ruiz-Pérez, Inorg. Chem. 47 (2008) 8053–8061.

[36] L. Shi, T. Wang, H. Zhang, K. Chang, X. Meng, H. Liu, J. Ye, Adv Sci 2 (2015) 1–8.

[37] J.Z. Gu, Y. Cai, X.X. Liang, J. Wu, Z.F. Shi, A.M. Kirillov, Cryst. Eng. Comm. 20 (2018) 906–916.

[38] A.F. Kateshali, S.G. Dogaheh, J. Soleimannejad, A.J. Blake, Coord. Chem. Rev. 419 (2020) 1–27.

[39] G.H. Cui, C.H. He, C.H. Jiao, J.C. Geng, V.A. Blatov, Cryst. Eng. Comm. 14 (2012) 4210–4216.

[40] O. V. Dolomanov, L.J. Bourhis, R.J. Gildea, J.A.K. Howard, H. Puschmann, J. Appl. Crystallogr. 42 (2009) 339–341.

[41] G.M. Sheldrick, Acta Crystallogr. Sect. A Struct. Chem. A71 (2015) 3–8.

[42] G.M. Sheldrick, Acta Crystallogr. Sect. C Struct. Chem. 71 (2015) 3–8.

[43] S. Chen, J. Qin, Z. Zhang, X. Cai, J. Gao, L. Liu, Zeitschrift Für Naturforsch. B 68 (2013) 277–283.

[44] C. Cai, Y. Tian, X. Ren, Y. Li, X. You, (2002) 924–927.

[45] V.A. Blatov, A.P. Shevchenko, D.M. Proserpio, Cryst. Growth Des. 14 (2014) 3576–3586.

[46] A.P. Shevchenko, A.A. Shabalin, I.Y. Karpukhin, V.A. Blatov, Sci. Technol. Adv. Mater. Methods 2 (2022) 250–265.

[47] C. Bonneau, M. O'Keeffe, D.M. Proserpio, V.A. Blatov, S.R. Batten, S.A. Bourne, M.S. Lah, J.-G. Eon, S.T. Hyde, S.B. Wiggin, L. Öhrström, Cryst. Growth Des. 18 (2018) 3411–3418.

[48] M.Sanselme, M.R.-C. J. M.Greneche, G. Ferey, Chem Commun (2002) 2172.

[49] H. Kumagai, K.W. Chapman, C.J. Kepert, M. Kurmoo, Polyhedron 22 (2003) 1921.

[50] S. Sharif, O. Sahin, I.U. Khan, O. Büyükgngr, J. Coord. Chem. 65 (2012) 1892–1904.

[51] S. Sharif, I.U. Khan, O. Sahin, S. Ahmad, B. Orhan, S. Ali, J. Inorg. Organomet Polym 22 (2012) 1165–1173.

[52] L.M. Zhao, B. Zhai, D.L. Gao, W. Shi, B. Zhao, P. Cheng, Inorg. Chem. Commun. 13 (2010) 1014–1017.

[53] A. Majumder, V. Gramlich, G.M. Rosair, S.R. Batten, J.D. Masuda, M.S. El Fallah, J. Ribas, J.P. Sutter, C. Desplanches, S. Mitra, Cryst. Growth Des. 6 (2006) 2355–2368.

[54] O. M.Yaghi, H. Li, T.L. Groy, Z.Kristallogr.-New Cryst.Struct. 212 (1997) 457.

[55] Millipore Sigma (2022).

[56] H. Hu, X. Lou, C. Li, X. Hu, T. Li, Q. Chen, M. Shen, B. Hu, New J. Chem. 40 (2016) 9746–9752.

[57] L.M. Bronstein, X. Huang, J. Retrum, A. Schmucker, M. Pink, B.D. Stein, B. Dragnea, Chem. Mater. 19 (2007) 3624–3632.

[58] Y.A. Barnakov, I.U. Idehenre, S.A. Basun, T.A. Tyson, D.R. Evans, Nanoscale Adv 1 (2019) 664–670.

[59] D.Q. Chu, C.L. Pan, L.M. Wang, J.Q. Xu, Mendeleev Commun. 12 (2002) 207–208.

[60] M. Halouani, M. Abdelhedi, M. Dammak, N. Audebrand, L. Ktari, Open J. Inorg. Chem. 03 (2013) 100–108.

[61] M. Sanselme, J.M. Grenèche, M. Riou-Cavellec, G. Férey, Solid State Sci. 6 (2004) 853–858.

[62] M. Zhang, L. Wang, T. Zeng, Q. Shang, H. Zhou, Z. Pan, Q. Cheng, Dalt. Trans. 47 (2018) 4251–

4258.

[63] A. Shoneye, J. Tang, Appl. Surf. Sci. 511 (2020) 145479.

[64] J.J. Du, Y.P. Yuan, J.X. Sun, F.M. Peng, X. Jiang, L.G. Qiu, A.J. Xie, Y.H. Shen, J.F. Zhu, J. Hazard. Mater. 190 (2011) 945–951.

[65] Y. Li, H. Zhang, P. Liu, D. Wang, Y. Li, H. Zhao, Small 9 (2013) 3336–3344.

[66] L.K. Vugt, S.J. Veen, E.P.A.M. Bakkers, A.L. Roest, D. Vanmaekelbergh, J. Am. Chem. Soc. 127 (2005) 12357–12362.

[67] S.K. Choi, S. Kim, S.K. Lim, H. Park, J. Phys. Chem. C 114 (2010) 16475–16480.

[68] R. Marschall, Adv Funct Mater 24 (2014) 2421–2440.

[69] S. Thulasi Karunakaran, R. Pavithran, M. Sajeev, S. Mohan Mohan Rema, Results Chem. 4 (2022) 100504.

[70] A.A. Abd El Khalk, M.A. Betiha, A.S. Mansour, M.G. Abd El Wahed, A.M. Al-Sabagh, ACS Omega 6 (2021) 26210–26220.

[71] F. Wang, F. Tian, Y. Deng, L. Yang, H. Zhang, D. Zhao, B. Li, X. Zhang, L. Fan, Cryst. Growth Des. 21 (2021) 4242–4248.

[72] A. Ali, M. Muslim, I. Neogi, M. Afzal, A. Alarifi, M. Ahmad, ACS Omega 7 (2022) 24438–24451.

[73] J.P. Dong, Z.Z. Shi, B. Li, L.Y. Wang, Dalt. Trans. 48 (2019) 17626–17632.

[74] T. Liu, L. Wang, X. Lu, J. Fan, X. Cai, B. Gao, R. Miao, J. Wang, Y. Lv, RSC Adv. 7 (2017) 12292–12300.

[75] M. Bertelli, E. Selli, J. Hazard. Mater. 138 (2006) 46–52.

[76] M. Hakimi, M. Alikhani, J. Inorg. Organomet. Polym. Mater. 30 (2020) 504–512.

[77] K.G.M. Laurier, F. Vermoortele, R. Ameloot, D.E. De Vos, J. Hofkens, M.B.J. Roeffaers, J. Am. Chem. Soc. 135 (2013) 14488–14491.

Supplementary Information

Photocatalytic degradation of methylene blue using sunlight-powered coordination polymers constructed from a tetracarboxylate linker

Adetola C. Oladipo[a,b], Abiodun D. Aderibigbe[c], Victoria T. Olayemi[b,d], Peter A. Ajibade[e], Hadley S. Clayton[f], Pavel N. Zolotarev[g], Guy J. Clarkson[h], Richard I. Walton[h] and Adedibu C. Tella[b,f]

[a]Department of Physical Sciences, Landmark University, P. M. B 1001, Omu-Aran, Kwara State, Nigeria

[b]Department of Chemistry, P.M.B.1515, University of Ilorin, Ilorin, Kwara State, Nigeria

[c]Department of Chemistry, Federal University of Technology, P.M.B. 704, Akure, Ondo state, Nigeria

[d]Department of Chemistry, College of Pure and Applied Sciences, Kwara State University, P.M. B 1530, Malete, Nigeria.

[e]School of Chemistry and Physics, University of Kwazulu-Natal, Scottsville, Pietermaritzburg, 3209, South Africa.

[f] Department of Chemistry, University of South Africa, South Africa

[g]Università degli studi di Milano, Dipartimento di Chimica, Via Golgi 19, 20133 Milano, Italy

[h]Department of Chemistry, University of Warwick, Coventry, CV4 7AL, UK

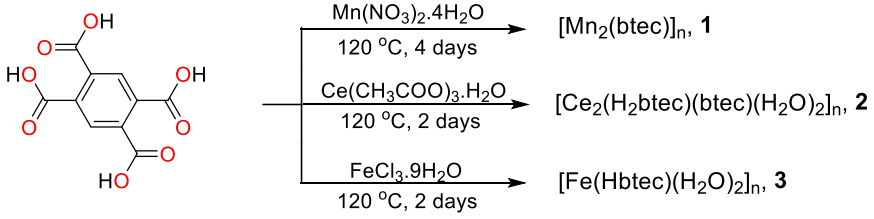

Figure S1. Synthetic routes to coordination polymers **1**, **2**, and **3**

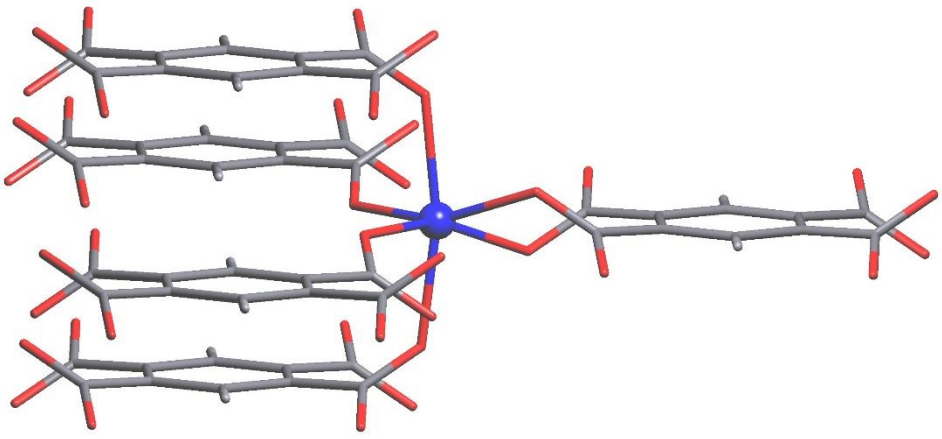

Figure S2: Coordination of the six coordinated Mn atom in **1** showing the overall connectivity to five different ligands: four terminal and one chelating.

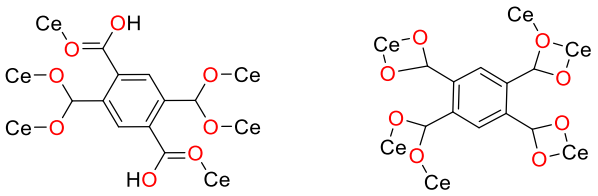

Figure S3. Coordination modes of btec ligand (a) H_2btec^{2-} ion; (b) $btec^{4-}$ ion in **2**

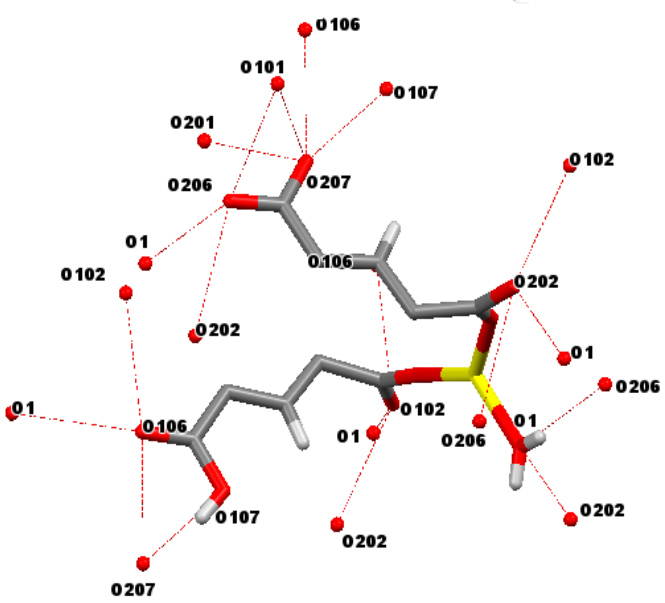

Figure S4. Asymmetric unit of **2**, showing the intermolecular hydrogen bonds

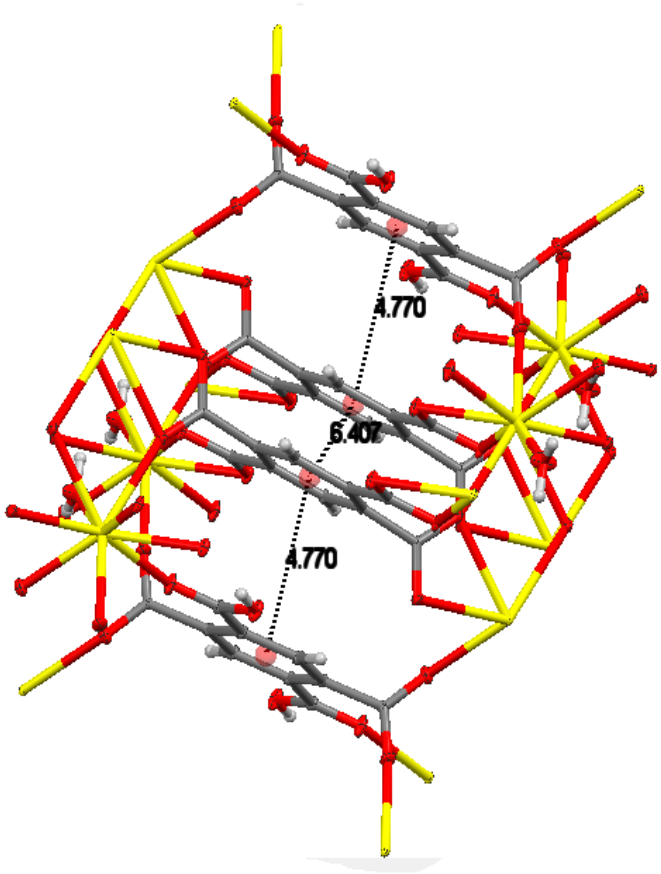

Figure S5. Packing of **2**, showing the high centroid-centroid distances

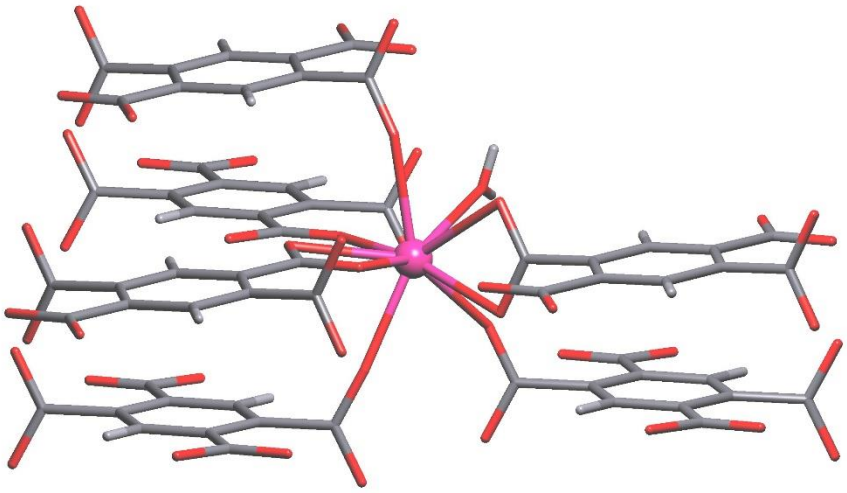

Figure S6: Coordination of the nine coordinated Ce atom in **2** showing the overall connectivity to six different ligands: three chelating and three terminal and one water molecule that does not contribute to the connectivity of the underlying net 6,6-**nia**

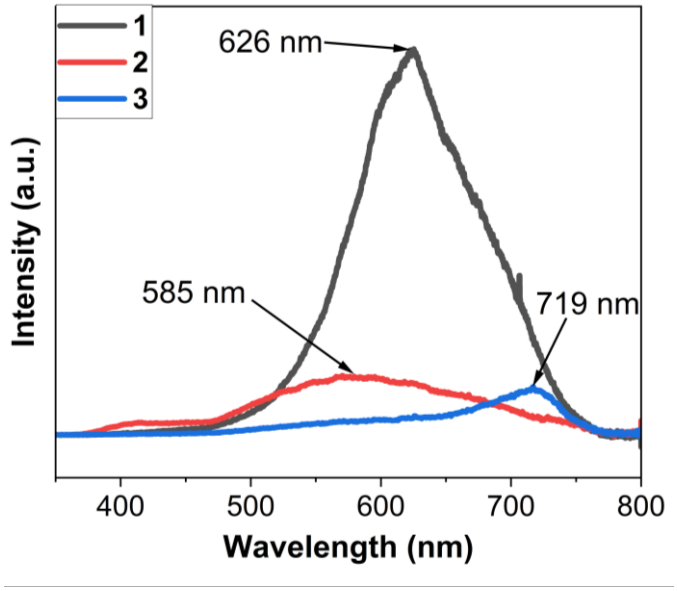

Figure S7. Photoluminescence spectra of **1**, **2**, and **3**

Table S1 Crystal data and structure refinement for **1** and **2**

Property	**1**	**2**
Empirical formula	$C_{10}H_2Mn_2O_8$	$C_{20}H_{10}Ce_2O_{18}$
Formula weight	360.00	818.52
Temperature/K	150(2)	150(2)
Crystal system	monoclinic	Triclinic
Space group	I2/m	P-1
a/Å	4.65500(10)	6.40680(10)
b/Å	17.7436(4)	9.3843(2)
c/Å	5.9991(2)	9.5404(2)
α/°	90	88.5030(10)
β/°	108.559(3)	74.564(2)
γ/°	90	76.662(2)
Volume/Å^3	469.74(2)	537.615(19)
Z	2	1
ρ_{calc}g/cm^3	2.545	2.528
μ/mm^{-1}	2.732	4.282
F(000)	352.0	390.0
Crystal size/mm^3	0.1 × 0.06 × 0.02	0.24 × 0.2 × 0.18
Radiation	MoKα (λ = 0.71073)	MoKα (λ = 0.71073)

2Θ range for data collection/°	7.524 to 69.244	6.172 to 69.46
Index ranges	$-7 \le h \le 7, -27 \le k \le 27, -9 \le l \le 9$	$-10 \le h \le 9, -14 \le k \le 14, -15 \le l \le 15$
Reflections collected	8922	32560
Independent reflections	1007 [R_{int} = 0.0393, R_{sigma} = 0.0203]	4435 [R_{int} = 0.0465, R_{sigma} = 0.0221]
Data/restraints/parameters	1007/0/48	4435/3/188
Goodness-of-fit on F^2	1.156	1.106
Final R indexes [I>=2σ (I)]	R_1 = 0.0212, wR_2 = 0.0606	R_1 = 0.0156, wR_2 = 0.0380
Final R indexes [all data]	R_1 = 0.0228, wR_2 = 0.0613	R_1 = 0.0160, wR_2 = 0.0382

Table S2: Bond length and angles for **1** and **2**

1		**2**	
Bond Length (Å)	**Bond Angle (°)**	**Bond Length (Å)**	**Bond Angle (°)**
Mn1-O2[1] 2.2369(9)	O2[1]-Mn1-O2[2] 79.06(5)	Ce1-O1 2.4761(12)	O1-Ce1- O106[1] 73.65(4)
Mn1-O2[2] 2.1670(9)	O2[3]-Mn1-O2[4] 167.66(5)	Ce1-O101 2.4075(11)	O1-Ce1- O201 70.19(4)
Mn1-O2[3] 2.2369(9)	O2[1]-Mn1-O2[4] 76.16(4)	Ce1-O102[1] 2.4487(11)	O1-Ce1- O201[2] 77.27(4)
Mn1-O2[4] 2.1670(9)	O2[2]-Mn1-O2[3] 76.16(4)	Ce1-O106[2] 2.5469(11)	O1-Ce1- O202[2] 102.99(4)
Mn1-O1 2.1143(9)	O2[1]-Mn1-O2[3] 113.88(3)	Ce1-O201[3] 2.6235(10)	O1-Ce1- O206[3] 145.54(4)
Mn1-O1[5] 2.1144(9)	O2[2]-Mn1-O2[4] 113.88(3)	Ce1-O201 2.5253(11)	O1-Ce1- O207[3] 129.87(4)
	O1[5]-Mn1-O2[3] 85.37(3)	Ce1-O202[3] 2.5332(10)	O101-Ce1- O1 141.13(4)
	O1-Mn1-O2[1] 155.84(3)	Ce1-O206[4] 2.5916(10)	O 206[3]-Ce1- O201[2] 74.61(3)
	O1[5]-Mn1-O2[2] 155.84(3)	Ce1-O207[4] 2.5626(11)	O 207[3]-Ce1- O201[2] 114.65(3)
	O1[5]-Mn1-O2[1] 94.72(3)		O207[3]-Ce1- O206[3] 50.53(3)

Symmetry operators:[1]1/2+x,1/2-y, -1/2+z; [2]3/2-x,1/2-y,3/2-z; [3]1+x,+y,+z; [4]1-x,+y,1-z; [5]2-x,+y,1-z; [6]-1+x,+y,+z; [7]+x,1-y,+z; [8]1-x,+y,2-z

Table S3: Selected hydrogen bond parameters of **2**

D	H	A	d(D-H)/Å	d(H-A)/Å	d(D-A)/Å	D-H-A/°
O107	H107	O207[1]	0.84	1.75	2.5774(15)	166.3
O1	H1A	O202[2]	0.815(15)	2.34(2)	2.8164(16)	117.9(19)
O1	H1A	O206[3]	0.815(15)	2.138(17)	2.8863(17)	153(2)

Table S4. Selected data and band assignments of the diffuse reflectance spectra for H_4btec ligand **1**, **2**, and **3**

Compound /ligand	Wavelength (nm)	Energy (cm^{-1})	Assignments
H_4btec	230, 298	434783, 335570	π-π^*, n-π^*
1	270, 304	370370, 328947	π-π^*, n-π^*
	407,520	245700, 192308	LMCT, $^6A_{1g} \rightarrow {}^4T_{1g}(G)$
2	256,315	390625,317460	π-π^*, n-π^*
	396	252525	LMCT
3	254,310	393701, 322581	π-π^*, n-π^*
	368	271739	LMCT

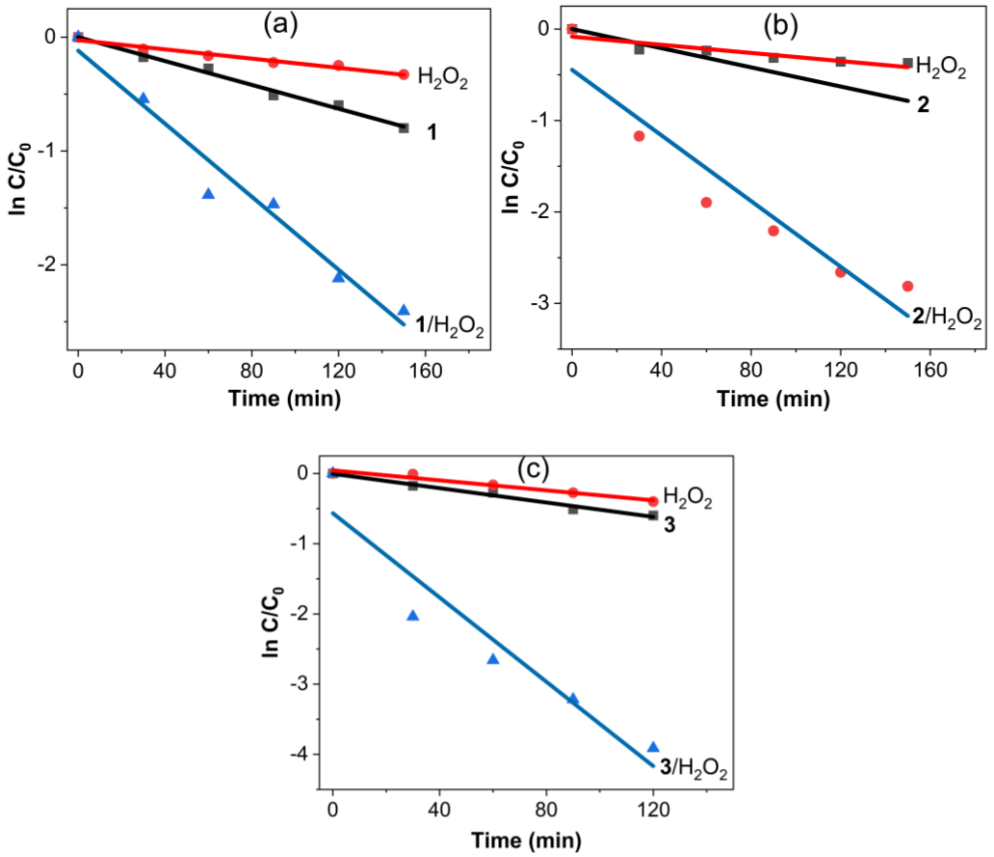

Figure S8. Comparison of the pseudo-first order plots of the (a) H_2O_2, **1**, and **1**/H_2O_2, (b) H_2O_2, **2**, and **2**/H_2O_2 and (c) H_2O_2, **3**, and **3**/H_2O_2 for the degradation of methylene blue

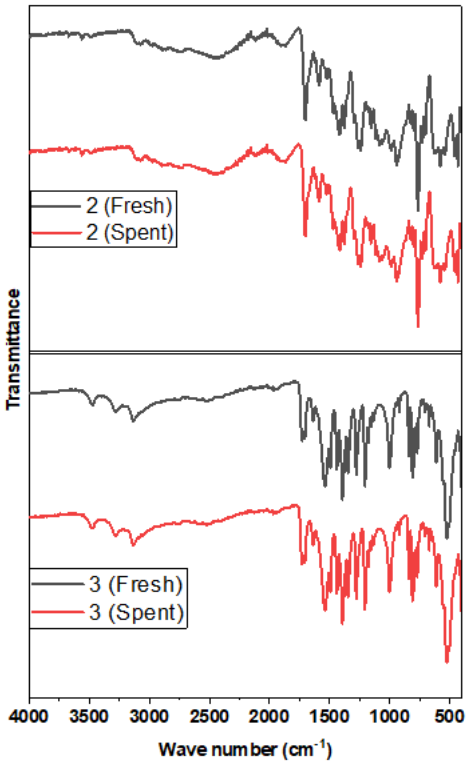

Figure S9. FT-IR Spectra of **2** and **3** before and after MB dye degradation